Towards strain gage 2.0

A Vinel, M Grédiac, X Balandraud, B Blaysat, T Jailin, Frédéric Sur

Towards strain gage 2.0. Substituting the electric resistance routinely deposited on polyimide film by the optimal pattern for full-field strain measurement

A. Vinel[1], M. Grédiac[1†], X. Balandraud[1], B. Blaysat[1], T. Jailin[1] and F. Sur[2]

[1] *Clermont Auvergne Université, CNRS, Clermont Auvergne INP, Institut Pascal, F-63000 Clermont-Ferrand, France*

[2] *LORIA, UMR 7503, Université de Lorraine, CNRS, INRIA, Nancy, France*
[†] *corresponding author, michel.grediac@uca.fr*

Abstract: The checkerboard constitutes the best pattern for full-field strain measurement because it maximizes image gradient. In the experimental mechanics community, employing this pattern is currently strongly limited because depositing it on the surface of specimens raises practical difficulties. A recent study shows that it is technically possible by using a laser engraver. The present paper aims to push this solution forward by printing the same pattern on a thin polymeric film, and then gluing the resulting laser-engraved film on the specimen surface. The underlying idea is to separate the manufacturing process of this optical strain gage on the one hand, and its use on the other hand, to help spread this strain measuring tool in the experimental mechanics community. The polymeric film employed here is the same as that used in the manufacturing process of classic electric gages, so one can rely on the know-how of classic strain gage bonding to glue this optical strain gage on the specimen surface. The main difference between the proposed tool and classic electric gages is that the strain field beneath the polymeric support is measured instead of pointwise strain values. The paper is a proof of concept for this strain field measuring tool. The manufacturing and bonding processes are described in the paper. The Localized Spectrum Analysis, a spectral technique developed for processing images of periodic patterns, is used to retrieve the strain fields from checkerboard images. Through two complementary examples, we show the ability of this new type of strain gage to detect and quantify local details in the strain field under it. A simplified 1D model is also proposed to assess the minimum width of the strain peak that can reliably be measured with this technique.

Keywords: checkerboard, crack, digital image correlation, full-field measurement, laser marking, localized spectrum analysis, optimal pattern, shape memory alloy, strain gage, wood

Introduction

Full-field measurement techniques are now widespread in the experimental mechanics community. Undoubtedly, the most popular one is Digital Image Correlation (DIC) [1]. This technique relies on surfaces marked with random patterns. With the classic version of DIC, the displacement is calculated pointwise at the center of the subsets used to mesh the zone of interest. DIC retrieves

this displacement by iteratively minimizing the so-called optical residual. In its simplest form, this quantity is the squared difference between the gray-level distributions of the images of the current and the deformed configurations. This minimization is performed subset by subset.

Defining the best pattern for such measurements is a key issue because the pattern carries the sought information. Optimizing this pattern in terms of metrological performance is the aim of several papers, see [2, 3, 4, 5, 6, 7, 8, 9, 10, 11] for instance. In the case of in-plane displacements and as discussed in [3], the best option is to use a periodic pattern such as a checkerboard, which is not random. Consequently, classic versions of DIC generally fail to find the displacement field with periodic patterns because of the presence of numerous local minima in the cost function to be minimized. A solution can be to use a special version of DIC called virtual DIC [11] or to switch the minimization of the optical residual from the spatial to the frequency domain [12, 13]. This latter option eventually leads to a quasi-direct link between the sought displacement and the phase change of the periodic pattern between current and reference configurations. The metrological performance is the same for these two approaches, but the second one is much faster [13], so it will be adopted in this study. The so-called Localized Spectrum Analysis (LSA) is used to extract the displacement and strain fields from the checkerboard pattern images discussed in this study. As discussed in [14], this is, with the Geometric Phase Analysis [15] and its windowed version [16], one of the spectral techniques which can be used to perform this task. It leads to a good tradeoff between calculation time and various parameters characterizing the metrological performance.

With such optimized patterns, a major hurdle is to deposit the tiny dots forming the checkerboard on the surface of the specimen to be tested, the challenge being to keep the size and the spatial distribution of those dots as regular as possible. It is, for instance, possible to print the pattern beforehand onto a polymeric sheet and then to transfer the black marking on the surface of interest by using a suitable white glue, as described in [17] for 2D grids, for instance. However, a printing device featuring a resolution greater than 10,000 dots per inch must be employed, which is much higher than that of classic office printers. In addition, complete adhesion is not always observed and tiny bubbles

in the glue may corrupt the regularity of the pattern. It is also challenging to keep a uniform and negligible thickness of the glue over the surface, which may cause the measurement technique to be intrusive in the case of high-strain gradients. Another route recently presented in [18] is to directly engrave the pattern on flat surfaces with a laser engraver, the surface being spray-painted in white beforehand. Indeed, the laser beam hits the coat of paint, and the color of the paint locally turns from white to black, eventually ensuring a good contrast between the black "printed" dots and the white layer of paint. Checkerboards with squares as small as 50 [μm] were engraved in the examples discussed in Ref. [18]. Further developments then enabled us to reduce this size to 30 [μm] [19]. However, the major disadvantage of this solution is that a laser engraver is quite expensive (55 keuros minimum when the engraver used in this study was purchased), which is a barrier to the diffusion of optimized patterns for displacement and strain field measurement in the experimental mechanics community.

The main contribution of this paper is to show that checkerboard patterns can be engraved on thin polymeric films, which can then be cut and bonded on the surface of any flat specimen. This piece of film is called the "optical strain gage" in the following. The underlying idea is to separate the manufacturing process of this optical strain gage on the one hand, and its use on the other hand, to help distribute this strain measuring tool in the experimental mechanics community, in particular to perform and develop tests within the framework of Material Testing 2.0 [20, 21]. A laser engraver is used to "print" tiny dots forming the checkerboard on the film. The polymer of the film used here is the same as that classically used as backing material for electric strain gages, namely polyimide (or Kapton® [22]). The advantage of using the same type of film is that one can rely on a bonding process similar to that used for bonding classic electrical gages, the latter being widely proven for strain measurement. The difference with classic electric strain gages is that this optical strain gage provides the strain distributions under it, and that its size is greater.

The paper is organized as follows. The materials and methods used to print and bond the optical strain gage are presented in Section 1. This also includes a brief description of how the images of such patterns are processed to extract displacement and strain fields. The results obtained with the optical

strain gage bonded on two different specimens are presented in Sections 2 and 3. They are made of a monocrystal of shape memory alloy and wood. In both cases, the main challenge is detecting and reliably measuring sharp details in the distributions under the optical strain gage. The experimental results are discussed, in particular, through the prism of an analytical shear-lag model, which predicts the "damping" of localized details caused by the presence of a film and a layer of adhesive. This discussion is in Section 4.

1. Materials and methods

1.1. Selecting the constitutive material for the optical strain gage

The first step of this study was to choose a suitable flexible support that meets different requirements. Indeed, the film must be:

1. Sensitive to the hit of the laser beam so that tiny dots forming the highest possible contrasted checkerboard pattern are visible after engraving.
2. Non-intrusive or as less intrusive as possible so that it reliably reproduces the state of strain under it on its free surface.
3. Easily bondable onto the specimen surface, the latter being assumed to be flat, at least for this first attempt.

Various stretchable and adhesive bandages, polymer stickers and tattoo papers were first unsuccessfully tested in a preliminary study (results not reported here). Checkerboard patterns could nearly systematically be successfully engraved after spray-painting these types of film in white. However, the problem was how to correctly tackle requirement 2 above in the case of high strain gradients because strain peaks were generally significantly "damped" by the presence of the film. For instance, this phenomenon was observed with the narrow martensite needles that appear in the shape memory alloy specimen discussed in Section 2 below. This hurdle was overcome by choosing the film routinely used to produce classic electrical strain gages. Indeed, electrical strain gages are generally obtained by etching constantan film and sealing it on a support made of polyimide. Therefore, the idea was to employ the

same backing material as that used for electric strain gages to benefit from the long experience gained when bonding them on flat surfaces. A 25 [μm]-thick polyimide film was used for this purpose. This film, supplied by ADDEV Materials, Saint-Chamond, France (`https://addevmaterials.com/en/`), is manufactured by DuPont [22]. It is worth mentioning that the raw color of polyimide is yellow/brown. Hence, such films shall be painted in white before engraving a pattern to have the highest possible contrast between the printed pattern and its background. To avoid this, the film that we employed was directly white in its bulk. In addition to avoiding painting the film, choosing a white film limits possible spatial fluctuations of the white color on the surface of the specimen.

1.2. Procedure for engraving checkerboard patterns on a white polyimide film

The procedure used to engrave a checkerboard pattern on a polyimide film is similar to that described in [18] to engrave the same type of pattern directly on the surface of specimens spray-painted in white beforehand. It relies on the use of a laser engraver. Some settings had, however, to be adjusted to avoid the film being pierced by the laser beam, or to be pierced with the smallest possible holes. Indeed, the glue may flow through the holes, which impairs the contrast of the printed side of the film. This may also cause some issues when removing the components used during the bonding process since they can potentially remain bonded on the pattern, see the following section for more details on the bonding procedure. A tradeoff had, therefore, to be found between laser power, the number of repetitions (in other words, the number of hits at the same place to progressively draw the dots), and the quality of the resulting contrast between black dots and white background. The settings used in this study are given in Appendix 1, along with those used to engrave a white paint layer directly deposited on the specimen surface. This second type of marking will be used in the examples below for comparison purposes.

1.3. Procedure for bonding the laser-engraved polyimide trip

A procedure similar to that used for bonding strain gages was followed to glue pieces of laser-engraved film forming the optical strain gage on the specimen surface. The glue employed here was a cyanoacrylate supplied by Micro-Measurement (Reference: M-bond 200). It is classically used to bond

electric strain gages. However, there are two main differences with classic electric strain gage bonding in the present application:

- The first difference is that the size of the optical strain gage to be bonded is here much greater than the average size of an electrical strain gage. For instance, the area covered by the optical strain gage reaches several cm^2 in the two examples discussed below (about 10 and 30 [cm^2], respectively). Hence, obtaining a regular layer of glue between the optical strain gage and the substrate is somewhat tricky. This justified the setting up of a procedure dedicated to bonding optical strain gages larger than classic electric gages.

- The second difference is that tiny details in the strain distribution under the piece of the laser-engraved film must be reliably revealed. In contrast, a classic gage returns only a mean strain value under the electric resistance. Consequently, the glue layer must be as thin as possible to limit the "damping" of the sharp details in the strain maps, and an important question is also to know to what extent the polyimide film also induces a damping of these details.

After different attempts, the best way to bond an optical strain gage on a flat specimen was first to place it on an adhesive tape with the printed face *against* the adhesive layer. This adhesive layer, made of flexible PVC to facilitate its deposition onto the engraved polyimide and limit tiny air bubbles to form between the two, serves two roles:

1. Engraving a pattern on such a thin film (thickness: 25 [μm]) causes the film to become brittle, so it easily tears. Depositing it on a flexible tape makes it easier to handle.
2. Glue flows out the adhesive joint while pressing the film onto the substrate, so the tape protects the printed surface against this excess glue.

The following procedure is used after depositing the film onto the adhesive tape, assuming it is rectangular. One of the four sides of the tape protrudes. It is stuck onto the specimen surface; see the left-hand side of Figure 1-(a) and -(b). The three remaining borders of the laminated film (tape+film) are kept free by cutting the excess tape. In the following step, they will allow the glue to flow outside

the room between the surface of the specimen and the film. A thin layer of glue is then deposited on the specimen surface, and the opposite side of the printed face of the optical strain gage is placed on it. The stack formed by the specimen, the glue, the optical strain gage, and the tape (see schematic view in Figure 1-(a)) is pressed with a steel block featuring one side slightly convex and the other flat. The convex surface is placed on the stack, protected by a thin plate of foam rubber (thickness: 3 [mm]) coated with a release (anti-adhesive) layer deposited with a pressure canister. This foam rubber behaves like a sponge soaked with anti-adhesive. Gently pressing and oscillating the block by hand for about one minute enables the excess glue to flow outside the bonded joint; see the three arrows in Figure 1-(b). The block is then returned, with its flat surface now pressing onto the stack, and the adhesive is allowed to cure at room temperature. Pressure is exerted by a clamp or a massive object while curing to reach the lowest and most possible uniform thickness for the adhesive layer after polymerization, see the schematic view in Figure 1-(a), where all the ingredients involved in the bonding process are reported. The adhesive tape is finally removed after curing and unclamping, and only the optical strain gage remains bonded on the specimen surface. Measuring the thickness of the specimen before and after this procedure and subtracting the thickness of the optical strain gage enables us to deduce the thickness of the glue in the bonded joint. This average thickness of the polymerized adhesive layer is equal to about 50 and 80 [μm] for the two specimens presented below, respectively.This thickness influences the ability of the present optical strain gage to return fine details in strain maps reliably; see Section 4 below.

1.4. A primer on the Localized Spectrum Analysis

We now briefly explain how checkerboard images are processed to extract the strain maps shown and discussed in the examples below. The so-called Localized Spectrum Analysis (LSA) was used here or this purpose. This is one of the spectral techniques employed to process periodic patterns [14, 23]. It is shown in [14] that it leads to the best tradeoff between different constraints. While DIC relies on the minimization, in the spatial domain, of the optical residual calculated on subsets of images of random patterns, LSA can be regarded as the minimization of the same quantity on images of periodic

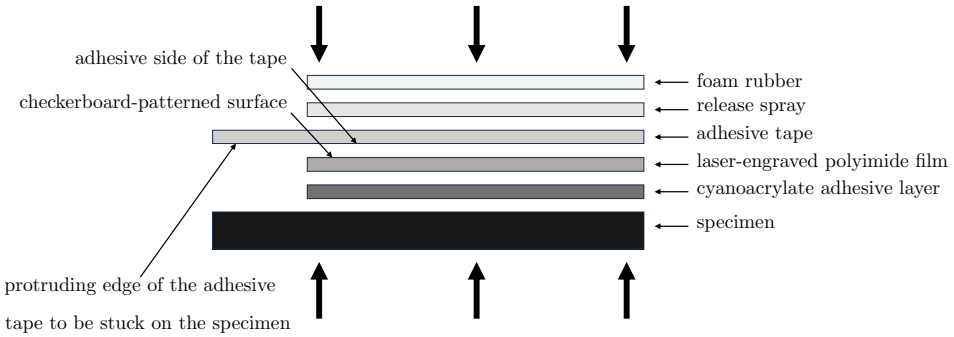

(a) Stack of constituents involved in the bonding process. Their thickness is not drawn to scale

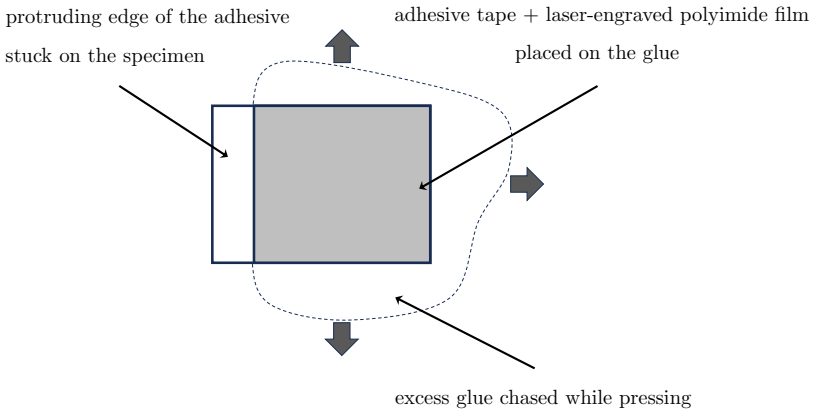

(b) Schematic top view illustrating the bonding process. The three arrows represent the excess glue chased while pressing the tape and the optical strain gage against the specimen surface

Figure 1: Schematic view illustrating the bonding process of an optical strain gage. The engraved surface is against the adhesive side of the tape. The other side is bonded onto the specimen surface.

patterns, but in the frequency domain [12]. The benefit is twofold: *i*- images of optimized patterns (in terms of metrological performance of the displacement/strain maps) such as checkerboards can be processed, and *ii*- the minimization is quasi-direct, thus avoiding the heavy calculations performed with the iterative minimization of the optical residual performed in the spatial domain with DIC. A consequence is that LSA returns displacement and strain maps pixelwise and less computationally demanding than DIC [14]. All details concerning this measuring technique can be found in Refs [24, 25], so we only briefly describe below the main steps of this technique.

The first step is to apply to the images of the pattern a Windowed Fourier Transform (WFT) with a unique frequency equal to the mean value of the period $\mathcal{P}$ of the checkerboard along the diagonals of the unit squares forming the pattern, see Figure 2-(a) below. The phase distributions for both the reference and the deformed images are then calculated by taking the argument of the result of the WFT (the WFT of an image gives a distribution of complex numbers defined at each pixel). The displacement field is finally deduced by using the following expression:

$$\underline{u}(\underline{x}) = -\frac{\mathcal{P}}{2\pi}\left(\underline{\Phi}^{cur}(\underline{x}+\underline{u}(\underline{x})) - \underline{\Phi}^{ref}(\underline{x})\right) \tag{1}$$

where $\underline{u}$ is the sought displacement field, $\underline{\Phi}^{cur}$ and $\underline{\Phi}^{ref}$ both contain two phase distributions, namely one along each direction of the reference and current images, respectively. $\underline{u}$ is involved in both parts of Equation 1. It is retrieved by using the fixed-point algorithm, which generally rapidly converges [24]. Directly subtracting the phase maps without performing this compensation of the displacement between current and reference images causes the parasitic fluctuation of the frequency of the checkerboard to impact the quality of the strain maps negatively.

The window used in the WFT is a 2D Gaussian function. Such a window gives the best tradeoff between various constraints [26]. The following equation gives the function defining this Gaussian window:

$$w(\underline{x}) = \frac{1}{2\pi\ell_{\mathsf{LSA}}^2} e^{\left(-\frac{||\underline{x}||^2}{2\ell_{\mathsf{LSA}}^2}\right)} \tag{2}$$

where ℓ_{LSA} is the standard deviation and $||\underline{.}||$ denotes the norm of vector "$\underline{.}$". This is a handy parameter that the user can adjust to decrease the noise level in the strain maps since the higher the value of ℓ_{LSA}, the lower the noise level in the maps. The price to pay is that the spatial resolution is impaired in proportion. Another remark is that at first approximation and regardless of the noise affecting the displacement and strain maps, the displacement and strain components retrieved at each pixel are not exactly their true respective counterparts, but the true phase value *convolved* by the window defined in Equation 2 [27]. This induces a blur of the details in the maps, especially in the strain maps, in which those details are generally sharper than in the displacement maps. It is worth noting that, up to a certain cutoff frequency, these maps can be restored with a dedicated deconvolution algorithm described in [28, 29], but this option was not used in this study. The minimum value of the standard deviation of the Gaussian window is equal to $\ell_{\mathsf{LSA}} = \mathcal{P}$ after [25]. This gives the lowest possible (thus the best) spatial resolution, but the effect of sensor noise on the final map is the highest. Note finally that the program used to process the images is available online, see [30] for a complete description.

1.5. Description of two complementary validation tests

Two different tests were performed to validate the proposed approach. Since this optical strain gage aims to measure the heterogeneous strain field underneath, we chose challenging cases for which strong heterogeneities occurred.

Two patterns were deposited on the specimens, i. e., with the optical strain gage on the one hand and a classic checkerboard pattern directly engraved on its spray-painted surface on the other hand. The strain maps obtained in the second case served as ground truth since this is the technique that has been used so far. Comparing the strain distributions obtained in each case enables us to assess to what extent the optical gage can return strain maps, which are similar to those returned by the engraved checkerboard. The first test was performed on a phase-transforming material, namely a shape memory alloy, subjected to a thermal load. The second one was a tensile test performed on a specimen of wood

in which a cracked knot is embedded.

2. Test #1: specimen in shape memory alloy

2.1. Material and method

Test #1 consisted of measuring strain fields on the surface of a disk specimen made of a single-crystal of $CuAl_{13.9}Ni_{4.6}$ (wt.%) shape memory alloy (SMA) subjected to temperature-induced phase transformation. The specimen had a thickness of 3 mm and a diameter of 33 mm. The alloy's chemical composition and the heat treatment were adjusted so that the specimen could be either austenite (A), martensite (M), or a mixture of both phases at room temperature, depending on the thermal history. In the present test, starting from a purely austenitic specimen, about 60% martensite was obtained by cooling to nearly 0°C. The microstructure that was observed was preserved after returning to room temperature. Full details on this type of experiment and a discussion on the observed phase transformation phenomena can be found in a recent paper [19]. The objective of the present study is to analyze the strain maps returned by the measurement system in the case of highly localized gradients. Indeed, considering that the austenite is the reference state (zero strain), martensite appearance in the form of needles or bands caused local strain values up to about ±4%. The values of the strain components depend on the band orientation, as the transformation strain tensors of the different bands are rotationally related. This leads to sharp interfaces with strain "jumps" in theory. At the present experiment's observation scale, the strain values in a given martensite band are expected to be constant or to gently spatially evolve (due to elastic strains potentially involved in addition to the phase transformation strain).

For the test, half the specimen was instrumented using the conventional method, *i.e.* first spray-painting in white and then engraving the checkerboard pattern (CKB #1). The other half was instrumented with the proposed optical gage (CKB #2). The repeatability of the A↔M transformation in this specimen is not perfect, but sufficient to rely on previous experiments discussed in [19] to know the orientation of some martensite bands. The border between the two marking types was placed perpendicularly to a set of parallel martensite bands. This enabled us to examine if the strain values

measured within them remain continuous when changing the type of marking, *i.e.*, when crossing the border between the two marking zones. It should be recalled that there are theoretically strain jumps of several percent at the transition between austenite and martensite. Hence, this situation is quite challenging for the polyimide film bonded over such interfaces. The main objective here is to see whether the strain distributions are similar for the two types of marking within the martensite bands. Such a property is reflected by bands or needles featuring similar “amplitudes" in strain. The second objective is to examine how the borders of these needles or bands, which should correspond to a strain discontinuity, are returned by the measurement system.

Two sets of images were taken in the reference configuration (undeformed austenite) at room temperature, one optimized for CKB #1 and the other for CKB #2. Only the exposure time changed from one case to another; see Table 1 providing the testing conditions. The same was done after cooling down to 0°C and returning to room temperature, *i.e.*, when the specimen was partially transformed to martensite (deformed configuration). The strain fields obtained on both halves were then merged to form a unique one over the whole specimen.

Finally, note that the small squares forming the checkerboard pattern were slightly inclined with respect to the borders of the pixel grid of the camera to avoid aliasing, the latter inducing parasitic fringes in strain maps; see [31] in the case of 2D grids. The corresponding tilt angle is reported in Table 1 for each type of marking.

2.2. Comparison between the checkerboard patterns obtained with the two procedures. Impact of contrast on sensor noise propagation

Figures 2-(a) and (-b) show typical close-up views of the two checkerboard patterns, obtained with the paint layer (CKB #1) and the optical strain gage (CKB #2), in the reference undeformed state. The latter is slightly brighter than the former.The histograms of gray levels associated with both patterns are shown in Figure 2-(c) and (d). For CKB #1, the histogram has a specific profile with three “bumps”, as already established and discussed in [25]. The aspect for CKB #2 is different, with a unique peak shifted towards the right because the pattern is slightly brighter than for CKB #1.

The brighter aspect of CKB #2 causes the noise expected in the strain maps to be slightly higher

	Test #1 (SMA)	Test #2 (wood)
Camera	Prosilica GT 6600	
Type of sensor	CCD	
Image resolution	6576×4384 pixels^2	
Gray depth	8 bit	
Acquisition rate	1 fps	
Patterning technique	Laser marking	
Type of pattern	Periodic (checkerboard)	
Type of load	Temperature change	Tensile force
Exposure time (paint layer, CKB #1)	5.0 ms	3.9 ms
Exposure time (optical strain gage, CKB #2)	7.5 ms	5.5 ms
Lens	TC16M048 Opto Engineering Telecentric lens	Nikon ED AF Micro Nikkor 200 mm 1:4 D
Magnification	0.75	
Aperture		f/8
Field of view	48.4×32.2 mm^2	69.7×46.5 mm^2
Image scale	1 pixel = 7.36 µm	1 pixel = 10.6 µm
Tilt angle θ (paint layer, CKB #1)	7.2°	1.5°
Tilt angle θ (optical strain gage, CKB #2)	6.0°	−0.3°
Stand-off distance	50 cm	70 cm
Period $\mathcal{P}$ used in LSA	5.8 pixels	4.0 pixels
Standard deviation ℓ_{LSA} of the Gaussian window used in LSA	$\ell_{LSA} = \mathcal{P} = 5.8$ pixels	$\ell_{LSA} = \sqrt{2} \times \mathcal{P} = 5.7$ pixels

Table 1: Experimental settings for Test #1 (Section 2) and Test #2 (Section 3)

because the higher the brightness at a given pixel, the higher the sensor noise [32, 33, 34]; see Figure 3 where the standard deviations of the noise in the strain component maps are reported (excluding outliers corresponding to localized marking defects). For a given strain component, the map of standard deviations was first deduced pixelwise from a set of 50 maps for each checkerboard pattern in the reference configuration; then, an equivalent and global standard deviation was deduced for each pattern. Note that those maps were obtained from independent pairs of images, thus from 100 images. It can be checked in Figure 3 that the noise affecting the ε_{xy} component is, as expected, about $\sqrt{2}$ lower than those measured for the ε_{xx} and ε_{yy} components. On average, the noise level for CKB #2 (optical strain gage) is about 10 % higher than for CKB #1 (paint layer). It can also be noted that the noise levels obtained here are significantly higher than those measured in [25, 35], but the sampling density, the camera, and the lighting systems were different in these two papers. In addition, the support of the standard deviation of the Gaussian window employed in the present test #1 is smaller than in

these papers to diminish (thus improve) the spatial resolution, which automatically increases the noise level; see also [12].

Apart from the difference in brightness, the main conclusion that can be drawn from Figures 2-(a) and (-b) is that both patterns have the desired aspect of a checkerboard.

2.3. Strain maps

Figure 4-(a) shows the specimen with the two checkerboard patterns. The bottom part corresponds to the pattern directly engraved on the paint (CKB #1), while the top part corresponds to the polyimide film first engraved and then bonded on the specimen (CKB #2). The ε_{xx}, ε_{yy} and ε_{xy} strain maps are shown in Figures 4-(b), 5-(a) and 5-(b), respectively. To limit the effect of the sensor noise, these strain maps were obtained using the mean phase maps of 100 images of the reference configuration and the mean phase maps of 100 images of the deformed configuration. A correction is introduced to get rid of solid-rigid like movements which potentially corrupt the phase maps because of micro-vibrations. This procedure is therefore different from merely directly averaging the stack of reference and the deformed images, the averaged image obtained in the latter case being potentially corrupted by these micro-vibrations [36].

Overall, no real difference can be noted between the global appearance of the maps obtained with both markings. The strain magnitudes are similar. So-called martensite "laminates", *i.e.* periodic layerings of two strain levels within the martensite bands, are visible at the bottom of the specimen where paint layer was used (CKB #1): see the red box in Figure 4-(a). In [19, 29], such laminates had also been observed in roughly the same area of the same specimen, employing a paint layer for the checkerboard pattern. Martensite laminates are classically revealed at much lower scales within any martensite band. In the present test, laminates are not visible in the top part of the specimen covered by the optical strain gage (CKB #2). In [19, 29], laminates were observed in the middle of specimen within a microstructure similar to the yellow-green "V"-shaped zone shown in the white box depicted in Figure 4-(b). This is not the case here using CKB #2. This result is discussed further in Section 4 below. At this stage, it is not possible to state whether the optical strain gage attenuates the potential

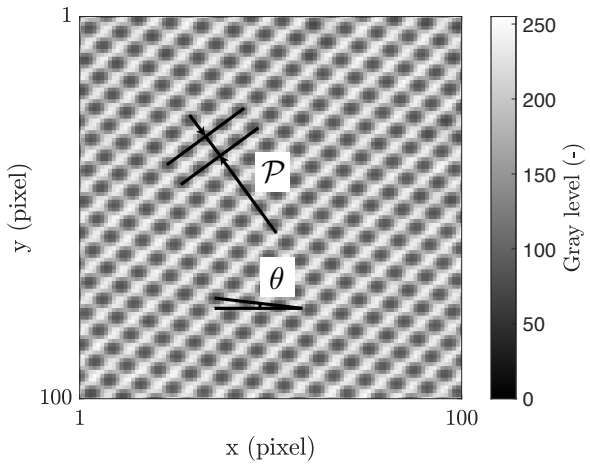

(a) Close-up view of CKB #1. Definition of $\mathcal{P}$ and θ used in LSA

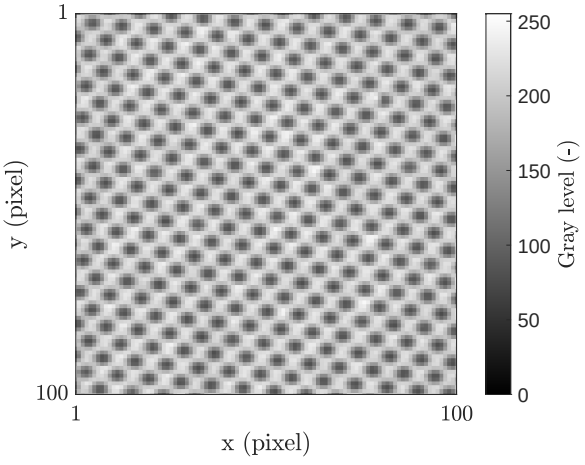

(b) Close-up view of CKB #2

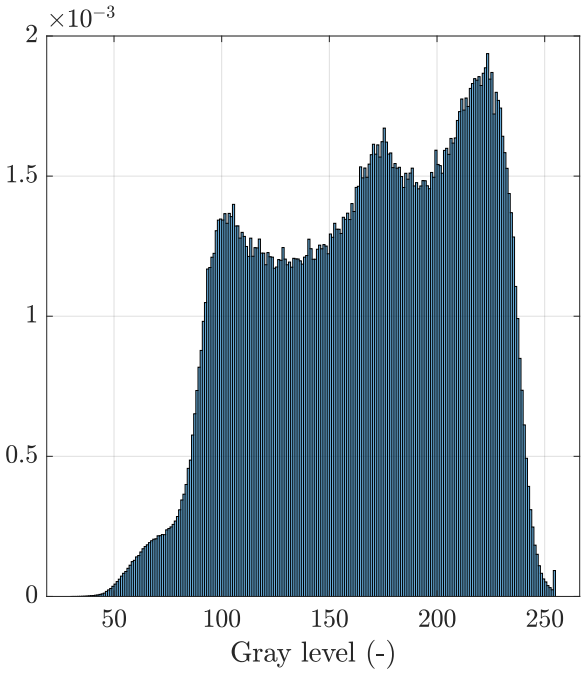

(c) Histogram for CKB #1

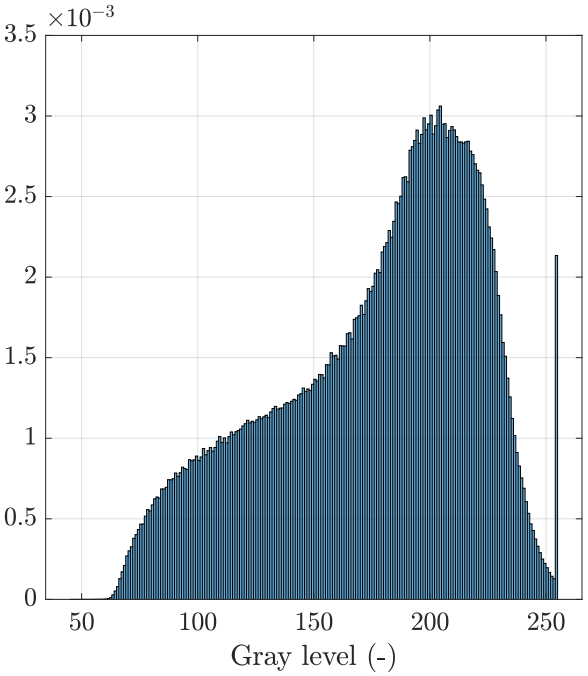

(d) Histogram for CKB #2

Figure 2: Checkerboard engraved on a layer of paint directly sprayed on the specimen surface (CKB #1) and its counterpart engraved on a polyimide film to form the optical strain gage bonded on the specimen surface (CKB #2). Close-up views and histograms of gray levels

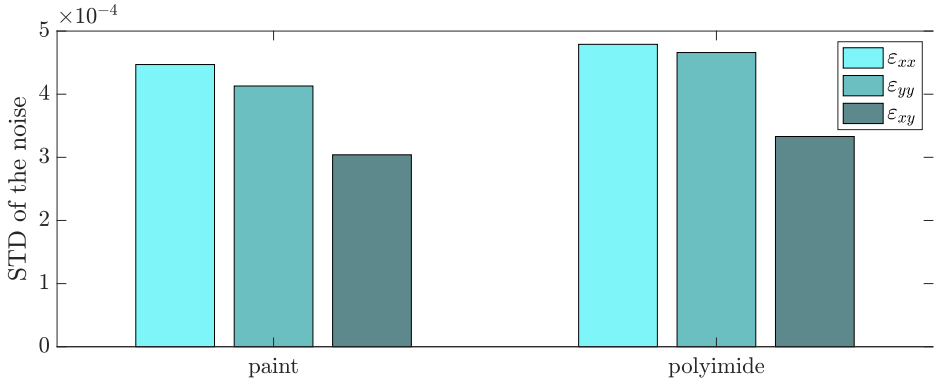

Figure 3: Standard deviation of the noise affecting the strain maps

periodic layering of two strain levels within the martensite bands in the top part of the specimen.

A close-up view of the ε_{yy} map obtained with both markings is depicted in Figure 6-(a). This zone corresponds to the black box in Figure 4-(a). The idea is to check, along a given martensite band, if the amplitude of the strain components measured within this band changes or not when crossing the border between each pattern. Indeed, this could be the illustration of a possible attenuation of the signal because of the presence of the optical strain gage. Various cross-sections of the ε_{xx}, ε_{yy} and ε_{xy} maps are plotted for this in Figure 6-(b)(c)(d), along the portions of lines shown in Figure 6-(a). The origin of each x'-axis is at the center of each portion of line, thus along the red line in Figure 6-(a). The width of this band, estimated at ε_{ij}=0, $ij = xx, yy, xy$, is equal to about 90 [px] = $90 \times 7.36 \times 10^{-3} \simeq 0.66$ [mm] on average. No attenuation of the signal is observed when going from the red to the blue curves for the ε_{yy} and ε_{xy} curves, their summit being nearly the same. The absolute value of ε_{xx} is even higher for the blue curves (CKB #1), than for the red ones (CKB #2) while a damping effect of the optical strain gage would give the contrary. This is certainly due to physical reasons. Indeed, it can be seen that the band at the top separates into two parts at the bottom, just after the border between the two patterns, and one of the two smaller bands is evanescent when going toward the bottom.

The strain profiles should be theoretically discontinuous at the interfaces between microstructures. This is not the case on the curves showing abrupt but not discontinuous changes in strain. This

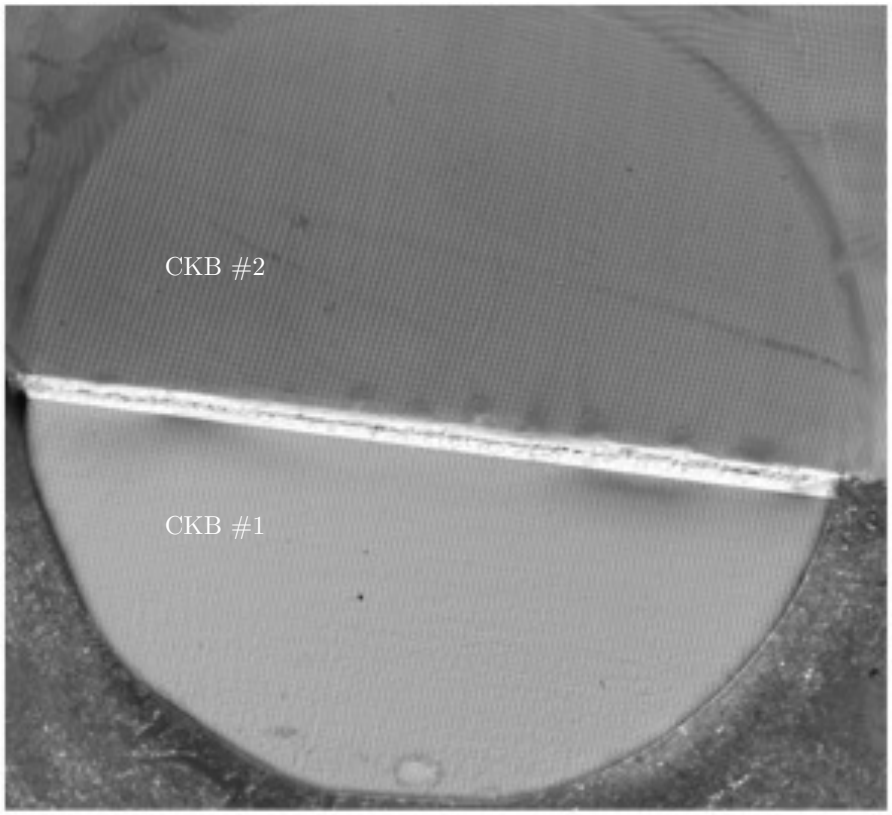

(a) Picture of the specimen marked with CKB #1 and CKB #2

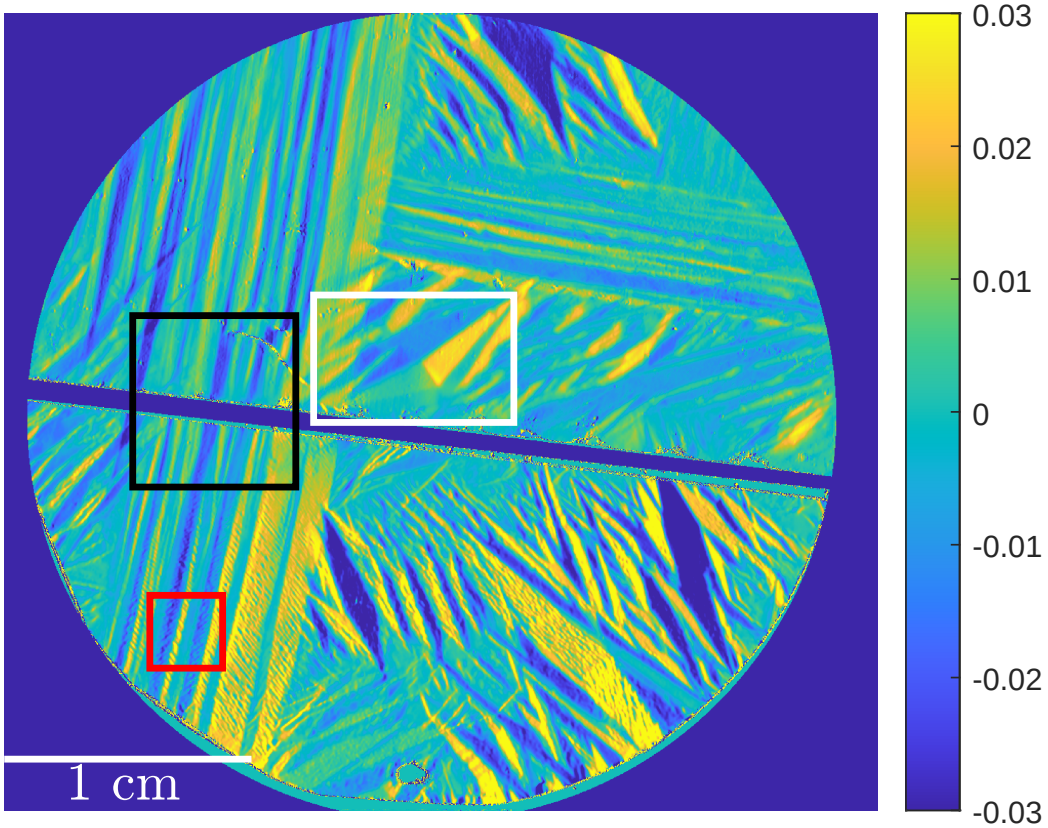

(b) ε_{xx}. The black box corresponds to the zone over which a close-up view is plotted in Figure 6(a)

Figure 4: Picture of the SMA specimen with the two patterns and ε_{xx} strain map. Bottom part of the specimen: CKB #1 (paint layer); Top part: CKB #2 (optical strain gage)

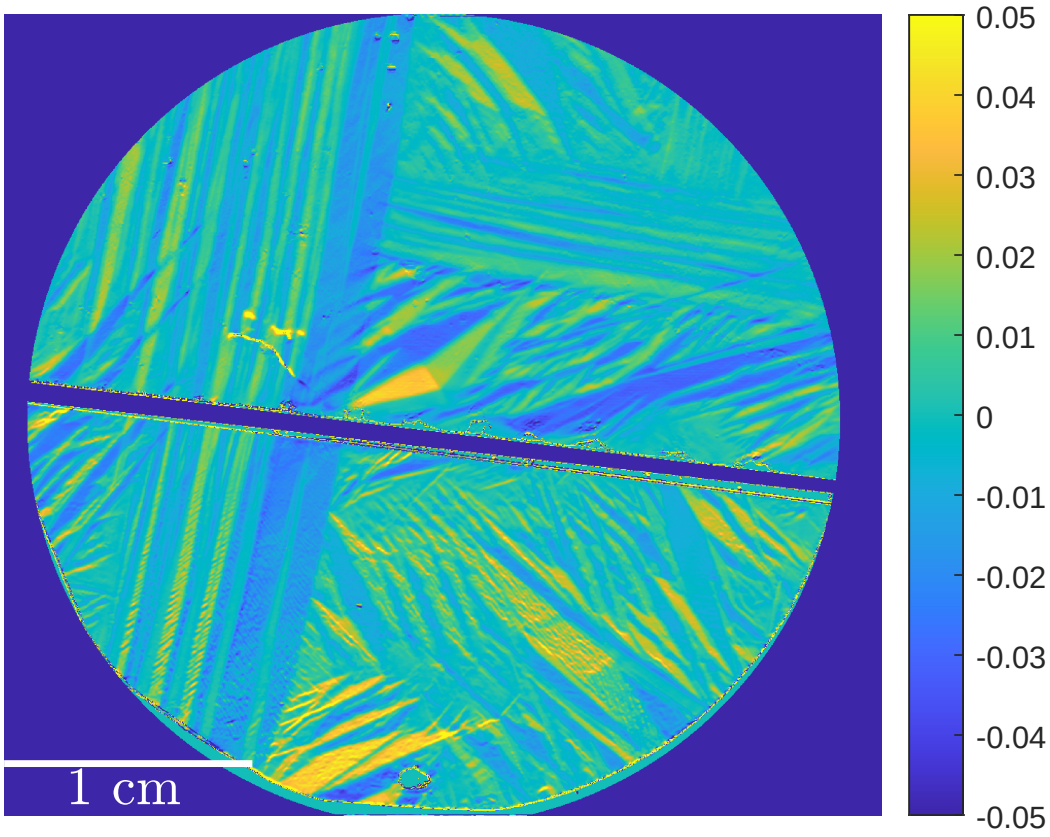

(a) ε_{yy}

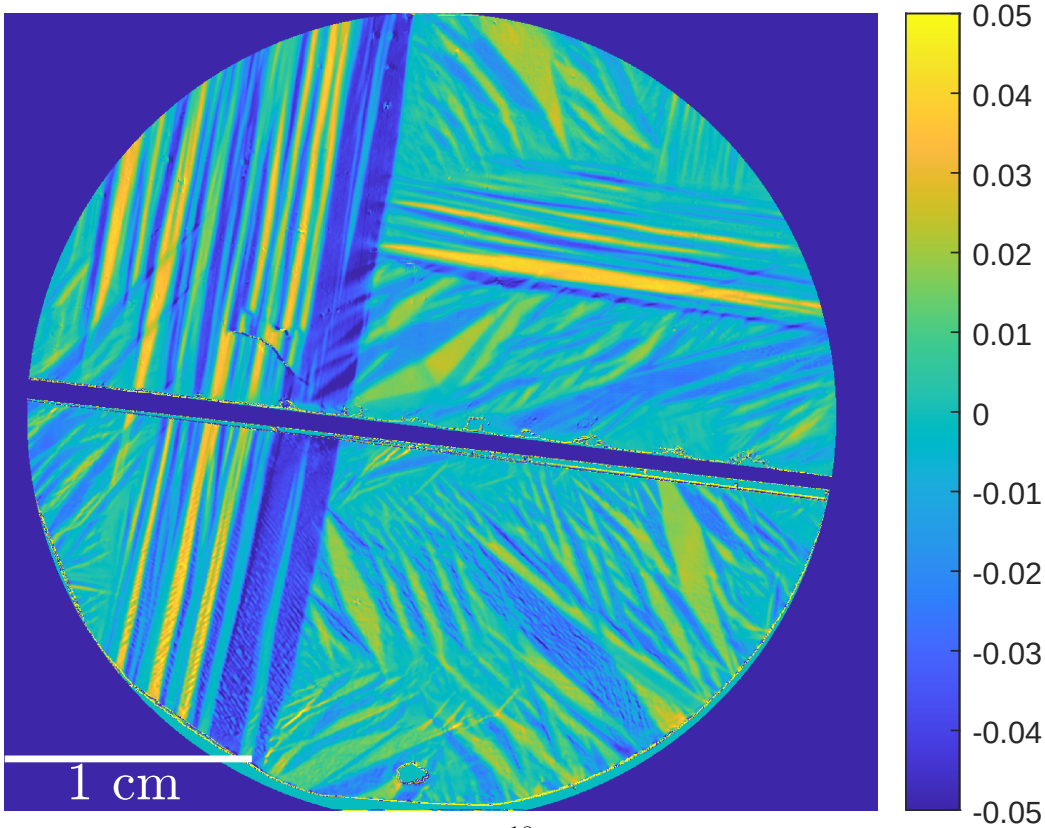

(b) ε_{xy}

Figure 5: ε_{yy} and ε_{xy} strain maps measured on the SMA specimen surface. Bottom part: CKB #1 (paint layer); Top part: CKB #2 (optical strain gage)

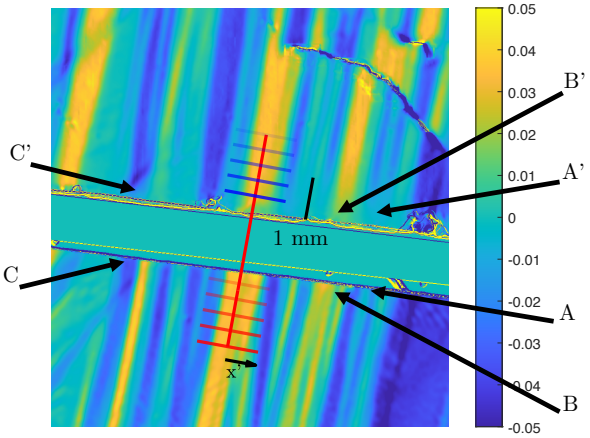

(a) Close-up view of the ε_{xy} map. Top: optical strain gage; bottom: paint layer

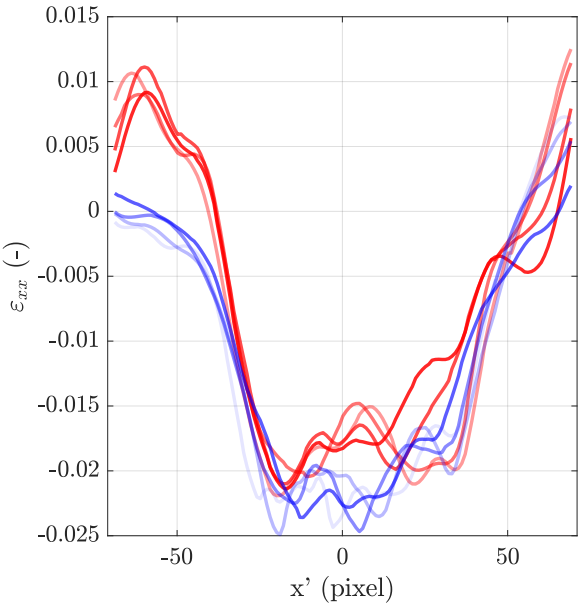

(b) ε_{xx}

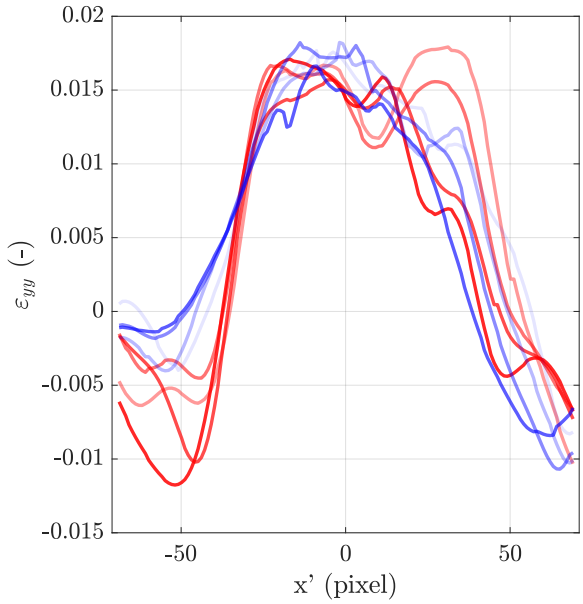

(c) ε_{yy}

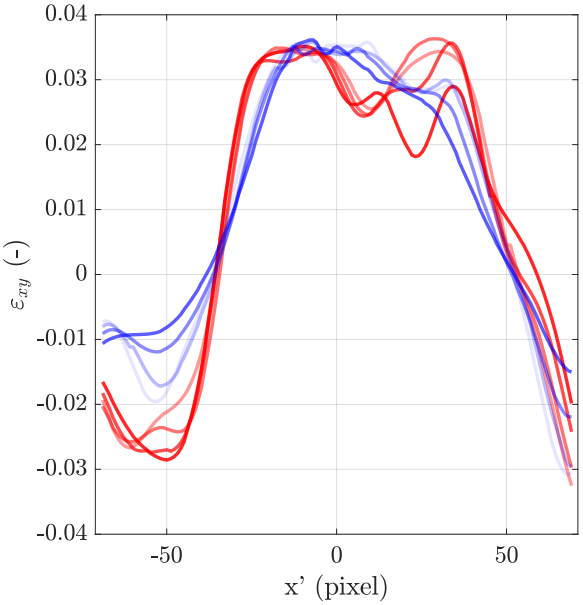

(d) ε_{xy}.

Figure 6: Analysis of the strain distributions measured in the black box in Figure 6-(a): (a) close-up view of the ε_{yy} strain map, showing the location of the line along which the cross sections are plotted. (b)-(d): strain profiles along the different cross-sections. Red: CKB #1 (paint layer). Blue: CKB #2 (optical strain gage).

illustrates the damping effect brought about by both the presence of the optical strain gage and LSA.

Another point is the fact that most of the needles/bands abruptly stop at the border of CKB #1 (see for instance Points A, B and C in Figure 4-(a)), while they progressively stop along the other side, thus at the border of CKB #2 (Points A', B' and C'). This point if discussed further in Section 4.

3. Test #2: cracked knot embedded in a wood specimen

3.1. Material and method

Test #2 was performed on a wood specimen. A knot crossed by a crack is embedded in it. Annual rings are also visible on the front face, in the zone where the optical strain gage is bonded. These features give rise to a heterogeneous strain field. The idea here is to see to what extent these heterogeneities can be detected in a configuration complementary to the preceding one. Indeed, if the specimen is tested in its elastic regime, the strain level is much lower than that reached with Test #1 (some 10^{-3} instead of some 10^{-2}). The impact of sensor noise propagation on strain maps is, therefore, higher.

Figure 7 shows the wood specimen. Its dimensions are $275 \times 45 \times 7.5$ [cm^3]. The red rectangle corresponds to the zone of interest. It surrounds the knot where the two checkerboard patterns were deposited in turn. Indeed, a first tensile test was performed after depositing the checkerboard pattern by spray-painting the external surface white and engraving the tiny black dots (CKB #1). The ultimate force (F = 3200 [N]) that was applied was such that the response of the specimen remained in the elastic regime. This corresponds to the deformed configuration for which the strain maps are below. The tensile machine used for this test was a Zwick/Roell UTS 20kN. After this first test, the specimen was sanded to remove the marked layer of paint. An optical strain gage (CKB #2) was then glued on the specimen. The latter was tested again by following the same procedure as that used in the preceding test, apart from the exposure time, which changed from one test to another (see Table 1) to have the highest possible contrast in the images for the pattern under interest. In this case, the quality of the two checkerboard patterns was similar to that of the two checkerboard patterns deposited in the preceding experiment. The physical size of the pitch remained unchanged, but the field of view

increased, which means that the number of pixels per period decreased in proportion.

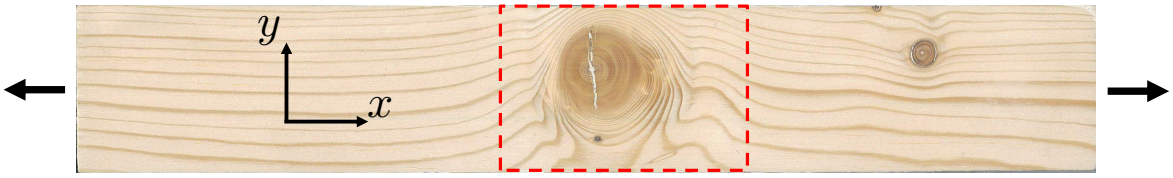

Figure 7: Wood specimen tested in this study. The red rectangle approximately corresponds to the zone over which the checkerboard patterns are deposited in turn, and thus strain maps are obtained. See the following figures where those maps are displayed after anticlockwise rotation of this zone by 90 degrees.

3.2. Results

Figures 8-9 show the distribution of the three in-plane strain components ε_{xx}, ε_{yy} and ε_{xy} over the red box in Figure 7 obtained during these two tests. There is a slight vertical shift between the maps displayed on the left and the right. The reason is that the specimen was removed from one test to another to change the type of marking. These maps are displayed in false color. Their size is $4262 \times 6457 \simeq 27.5 \times 10^6$ [px], or 4.5×6.8 [cm^2]. A close-up view of the zone of interest is also displayed in Figure 9-(c) for comparison purposes between the features in the maps and the picture (annual rings, crack, knot).

The standard deviation of the Gaussian window used in LSA to obtain these maps is chosen here to be equal to $\sqrt{2} \times \mathcal{P}$ instead of $\mathcal{P}$ with Test #1. This choice is justified by the fact that the sampling density of the periodic pattern is smaller with Test #2 than with Test #1. The Gaussian window is therefore chosen to be slightly greater (in pixel) to limit the noise level in the strain maps. Note that $\sqrt{2} \times \mathcal{P}$ is also twice the size of one unit square forming the checkerboard pattern.

According to the "3-sigma rule" [37], the Gaussian window used in LSA has an apparent area equal to the area of a disk with a diameter equal to six times the standard deviation, thus $5.7 \times 6 \simeq 34.2$ [px]$\simeq 34.2 \times 10.6 \times 10^{-3} \simeq 0.36$ [mm] in the present case. With LSA, the phases and the displacements are calculated pixelwise, but over a zone that is, roughly speaking, equal to this disk. The gradient function available in the NumPy library of Python was used to differentiate the displacement to deduce the strain components relies on the central difference approximation. The strain components are therefore estimated over a disk with a size equal to $5.7 \times 6 + 2$ [px]$\simeq 34.2 + 2$ [px]$\simeq$

$36.2 \times 10.6 \times 10^{-3}$ [mm]$\simeq$ 0.38 [mm]. It is plotted to scale in Figure 8-(d). With the present example, without taking border effects into account for simplicity, each strain map can be regarded as a set of results obtained with 27.5 millions of circular strain gages of diameter 0.38 [mm]. These local gages are centered at all the pixels. Consequently, each local strain gage is shifted by 1 [px] = 10.6 [μm] from the other along both directions. This shift causes a substantial overlap between these local gages, which explains that sharp strain gradients (at the scale of these tiny distances) may be blurred in the strain maps. Employing a dedicated deconvolution algorithm limits this negative effect [28, 29], but it was not necessary in the present case.

The calculation time needed to retrieve the three strain maps from a pair of images was 160 seconds with a PC (Intel 8-core, i9-11950H @ 2.60Ghz), which seems quite reasonable given the size of the maps. This is because the calculations performed with LSA are nearly straightforward and partly performed in the Fourier domain; see [24, 38, 13] for more details.

When observing these maps, the striking point is that they are similar from one type of marking to another. On close inspection, some slight differences can be detected, particularly concerning the sharpness of the details (effect of annual rings, for instance). Still, these details are more pronounced either in the left- or in the right-hand maps, depending on the zone that is considered. This is probably because the thickness of the paint layer on the left and the thickness of the adhesive on the right may spatially fluctuate; thus, the damping of the actual signal may also spatially fluctuate. Another point is that the thickness of the paint layer is higher here (150 [μm]) than in the preceding case (85 [μm]), which certainly induces additional damping with CKB #1 in Test #2 compared to Test #1. This is due to the higher roughness of the wood specimen surface than that of the SMA specimen, which causes additional spray paint layers to be deposited before obtaining a surface sufficiently smooth to be laser-engraved. It should also be noted that these maps were obtained with two separate tests, and the specimen was removed from the tensile machine from one test to another. Consequently, the loading conditions (positioning the specimen in the grips, clearance compensation) were not exactly the same from one test to another. Another point is the close correspondence between the features

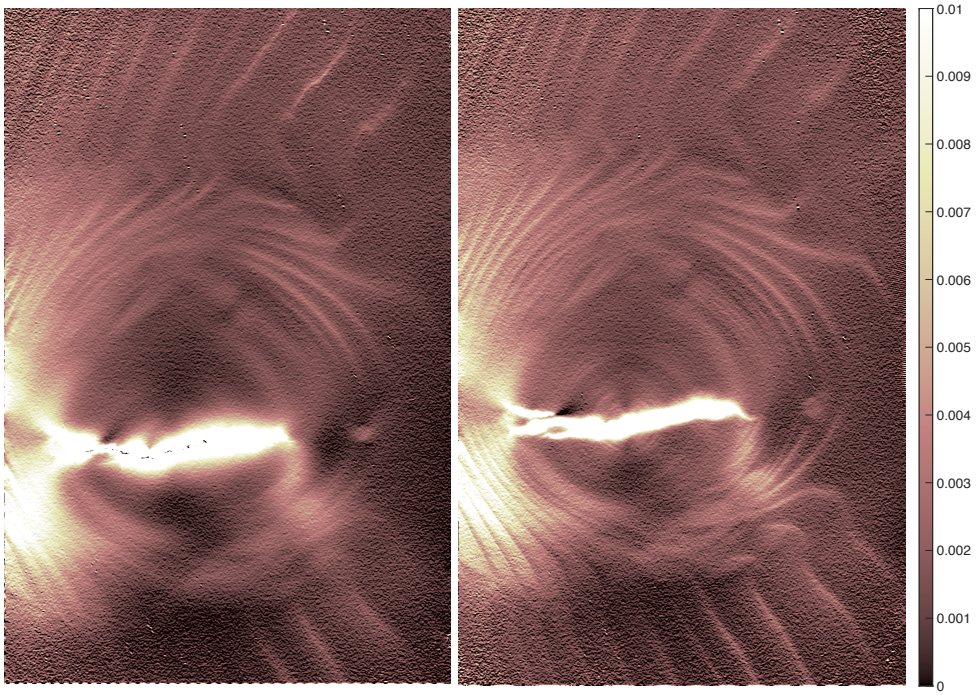

(a) ε_{xx} [-], CKB #1

(b) ε_{xx} [-], CKB #2

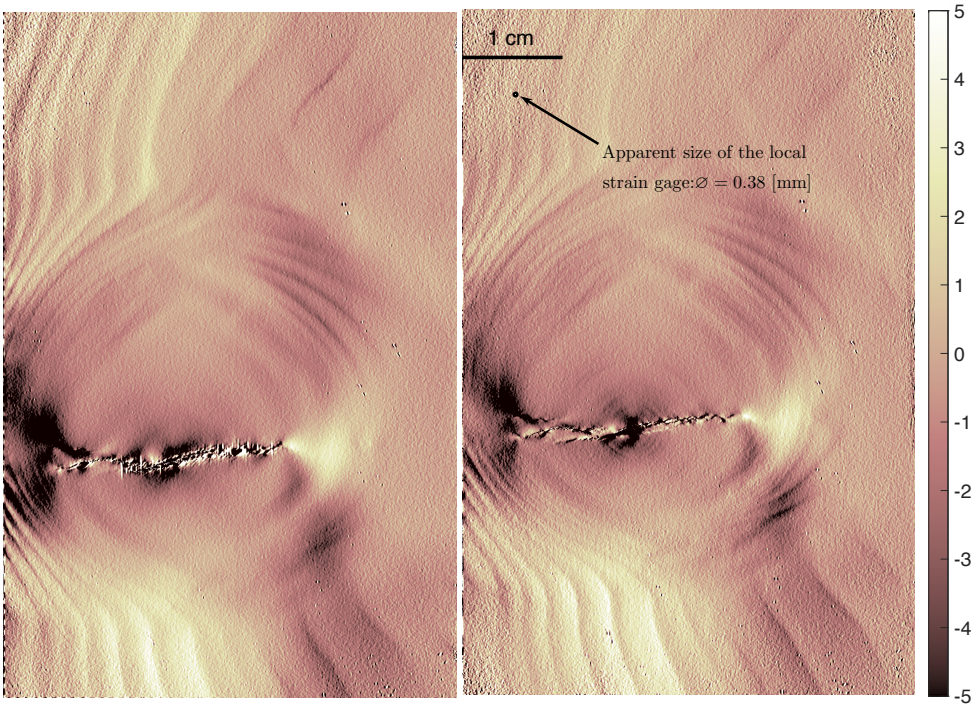

(c) $\varepsilon_{yy}(\times 10^{-3})$ [-], CKB #1

(d) $\varepsilon_{yy}(\times 10^{-3})$ [-], CKB #2

Figure 8: ε_{xx} and ε_{yy} maps plotted over the red box in Figure 7 for both types of patterns. Size: $4262 \times 6457 \simeq 27.5 \times 10^6$ [px]. (d): the small circle represents the apparent size of the local strain gage around any pixel of the map. Its diameter is equal to 36.2 [px]$\simeq$0.38 [mm].

(a) $\varepsilon_{xy}(\times 10^{-3})$ [-], CKB #1

(b) $\varepsilon_{xy}(\times 10^{-3})$ [-], CKB #2

(c) Zone of interest (red box in Figure 7)

Figure 9: ε_{xy} maps plotted over the red box in Figure 7 for both marking techniques. Comparison with a picture of the zone of interest

observed in the picture of the zone of interest in Figure 9-(c) and in the measured strain maps, see, for instance, the shape of the annual rings or the shape of the crack. The singular distribution of the strain components near the crack tip is also noticeable for the strain maps obtained with both patterns, mainly for the ε_{yy} component (see Figures 8-(c)-(d)). It is also worth noting that the annual rings within the knot do not lead to significant strain fluctuations in this zone, which is not the case outside the knot. This is undoubtedly because the wood within the knot is stiffer than its counterpart outside it. Finally, the noise effect is not pronounced on these maps. It is mainly visible near the corners of the maps. It can be checked that the pattern is less contrasted in the corresponding zones. Possible causes are the non-uniformity of the lighting because of the relatively large zone of interest, the fact that the front face of the specimen is not rigorously flat because of the successive sandings that were applied to remove the markings applied in turn or the fact that the effect of the marking defects is less correctly taken into account near the corners than at the center because of the distortion of the lens, which was not accounted for here. Indeed, since the lens used for this test is not telecentric, the depth of view is limited, which may slightly induce a blur in some zones of the images and thus impair the contrast.

4. A simplified model for the strain distribution along the gage in the presence of a sharp detail in the substrate

4.1. Description of the model

The strain distribution in the optical strain gage when a sudden strain change occurs in the substrate located just below is modeled here. Bearing in mind that LSA alone also causes a damping of the actual strain values, the objective is to have an idea of the size of the tiniest detail that can be reliably measured in a strain map when the optical strain gage is employed. We consider for this the simplified 1D model shown in Figure 10-(a).

This is a substrate covered by a layer of adhesive and the optical strain gage. This substrate is split into three domains, namely domains $\mathcal{D}_1$, $\mathcal{D}_2$ and $\mathcal{D}_3$. $\mathcal{D}_3$ is symmetric to domain $\mathcal{D}_1$ with respect to the vertical line Δ plotted at the middle of domain $\mathcal{D}_2$. Domain $\mathcal{D}_2$ models a singularity. This is a portion of the substrate where the Young's modulus suddenly drops. This causes strain jumps in the

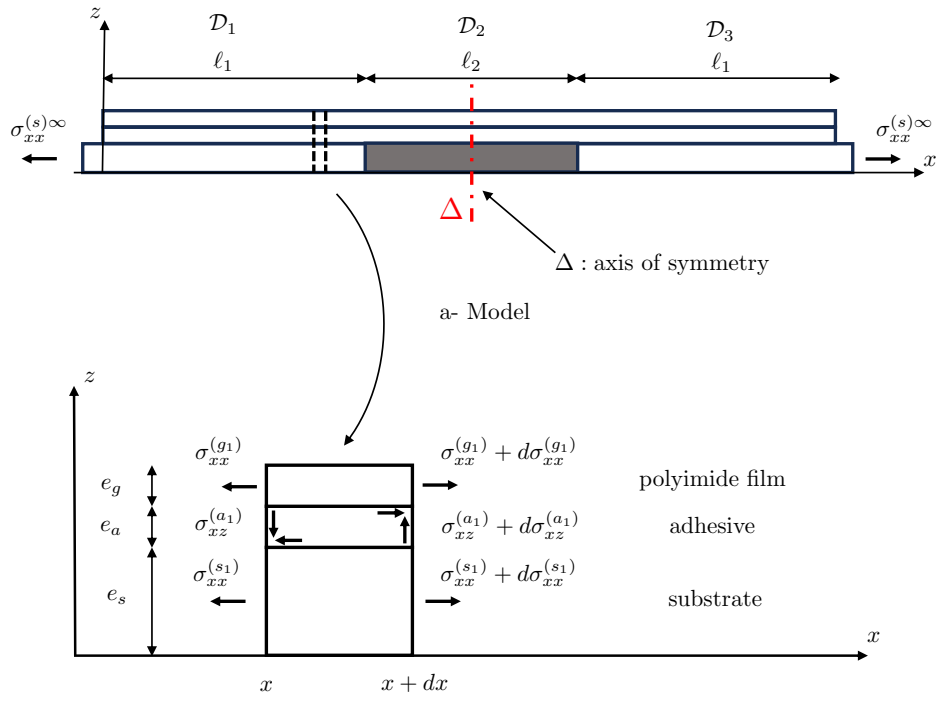

b- Slice of domain $\mathcal{D}_1$

Figure 10: Substrate covered by the adhesive and the optical strain gage.

substrate, mimicking those existing in Test #1 with the SMA specimen at the microstructure interface, or in the wood specimen perpendicularly to the annual rings. Under some suitable assumptions, it can be shown that the following equations give the strain distribution along the optical strain gage:

$$\begin{cases} \varepsilon_{xx}^{(g_1)} = \dfrac{1}{E_1}\left(K_1 e^{\gamma_1 x} + L_1 e^{-\gamma_1 x} + \dfrac{\beta_1}{\gamma_1^2}\right) \text{ over domain } \mathcal{D}_1 \\ \varepsilon_{xx}^{(g_2)} = \dfrac{1}{E_2}\left(K_2 e^{\gamma_2 x} + L_2 e^{-\gamma_2 x} + \dfrac{\beta_2}{\gamma_2^2}\right) \text{ over domain } \mathcal{D}_2 \end{cases} \tag{3}$$

where $\varepsilon_{xx}^{(g_i)}$ is the strain in the optical strain gage in domain $\mathcal{D}_i, i = 1, 2, 3$. $\varepsilon_{xx}^{(g_3)}$ over domain $\mathcal{D}_3$ is deduced from $\varepsilon_{xx}^{(g_1)}$ by mirror symmetry. For the sake of readability and compactness, the calculations leading to this result as well as the expressions giving $K_1, K_2, L_1, L_2, \gamma_1, \gamma_2, \beta_1$ and β_2 as a function of the dimensions of the specimen and the material properties are given in Appendix 2. This model enables us to examine the influence of different parameters on the strain distribution along the gage.

4.2. Damping effect induced by the presence of a sharp detail in the substrate

Figure 11 shows the ratio denoted by r_ε between the normal strain in the gage $\varepsilon_{xx}^{(g_i)}$, $i = 1, 2, 3$ (for domains $\mathcal{D}_1$, $\mathcal{D}_2$ and $\mathcal{D}_3$), and the strain that would take place in domain $\mathcal{D}_2$ without the gage. This quantity is equal to $\frac{\sigma_{xx}^{\infty}}{E_2}$. The r_ε ratio, thus equal to $r_\varepsilon = \frac{E_2 \varepsilon_{xx}^{(g_i)}}{\sigma_{xx}^{\infty}}$, is equal or lower than one. Over $\mathcal{D}_2$, $r_\varepsilon - 1$ reflects the extent to which the strain measured in the gage is affected by the presence of the optical strain gage in case of localized change of the strain in the substrate. Over $\mathcal{D}_1$ and $\mathcal{D}_3$, $r_\varepsilon < 1$ reflects the fact that $\frac{E_1}{E_2} > 1$, thus that $\varepsilon_{xx}^{(g_1)}, \varepsilon_{xx}^{(g_3)} < \frac{\sigma_{xx}^{\infty}}{E_2}$. The values of the parameters used to plot these curves are reported in Table 2. E_1, G_a are representative of the different materials involved in Test #1 above, e_s, e_a, e_g of the thickness measured on the corresponding specimen. $E_1 = 120$ GPa is the order of magnitude of the Young's modulus of the austenite [39]. G_a is deduced from the Young's modulus given in [40] (1.26 GPa), assuming the Poisson's ratio is equal to 0.30 [-]. E_g is the value given in the datasheet of the polyimide supplier [22]. The value of E_2 is significantly lower than E_1 ($r_E = \frac{E_1}{E_2} = 24$) to model a sudden softening of the substrate, thus a sudden strain peak in this substrate since the ratio between the longitudinal strain in $\mathcal{D}_2$ and $\mathcal{D}_1$ is equal to $\frac{E_1}{E_2}$, the model being unidimensional. This induces a ratio between the strain levels similar to austenite and martensite in Test #1. The objective here is to observe the influence of the width of this singularity, namely ℓ_2, on the r_ε ratio, ℓ_2 spanning the [0,1] [mm] interval to include the values for which the longitudinal strain drops.

Figure 11 shows that the strain distribution in the optical strain gage, normalized by $\frac{\sigma_{xx}^{\infty}}{E_2}$, continuously changes (for the sake of continuity of the film). It is nearly constant over some zones and features some abrupt changes, first near both the free borders, and at the border between $\mathcal{D}_1$ and $\mathcal{D}_2$ on the one hand, and between $\mathcal{D}_2$ and $\mathcal{D}_3$ on the other hand. Near the borders, this phenomenon can be represented by a classic shear lag model [41]. At the boundaries between the different domains, the optical strain gage "accommodates" the sudden strain change in the substrate. Hence, a transfer zone also occurs at these two places. This causes a decrease of the strain peak, thus of the r_ε ratio, if the length of domain $\mathcal{D}_2$, namely ℓ_2, becomes lower than a particular threshold value. With the present

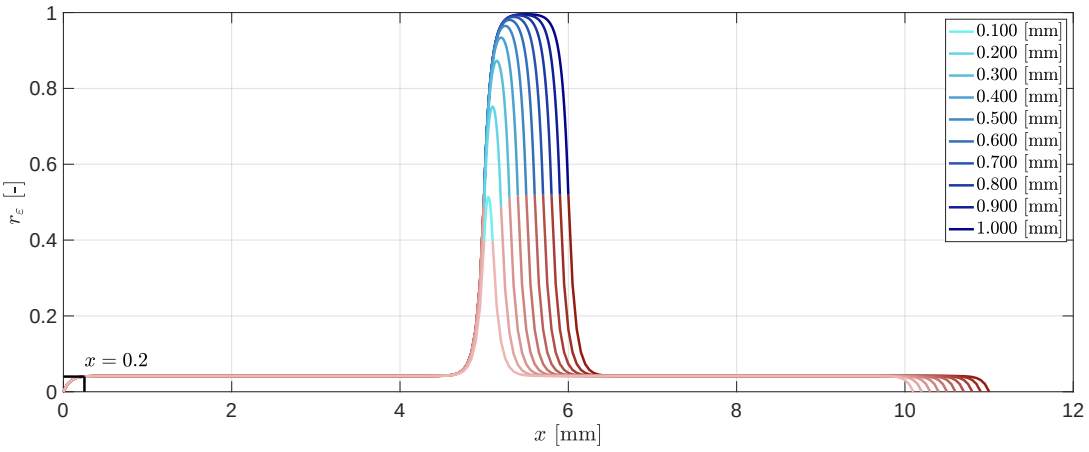

Figure 11: Ratio $r_\varepsilon = \frac{E_2 \varepsilon_{xx}^{(g_i)}}{\sigma_{xx}^{\infty}}$, $i = 1, 2, 3$ for domains $\mathcal{D}_1$ ($0 \leq x \leq 5$ mm), $\mathcal{D}_2$ (5 mm $\leq x \leq 5$ mm + ℓ_2) and $\mathcal{D}_3$ (5 mm + $\ell_2 \leq x \leq 10$ mm+ ℓ_2), respectively, and for various values of ℓ_2 reported in the legend. Red: domains $\mathcal{D}_1$ and $\mathcal{D}_3$. Blue: domain $\mathcal{D}_2$. The brighter the color, the lower the value of ℓ_2. The values of the parameters governing the model are reported in Table 2.

values of the parameters governing the model, the curves plotted in Figure 11 show that the r_ε ratio begins to decrease for a value of $\ell_2 \simeq 0.7$ mm. A loss of amplitude of r_ε equal to 10 % is reached for a value of ℓ_2 lying between 0.3 and 0.4 mm.

These curves were obtained for a particular value of the $r_E = \frac{E_2}{E_1}$ ratio. Thanks to the model, we can generalize this result by considering a changing value for both the r_E ratio and ℓ_2. ℓ_2 still spans the [0,1] [mm] interval. r_E lies now between 2.5% and 80% instead of being constant, with a step equal to 2.5%. The other parameters remain unchanged. For all values of r_E, we collected the maximum value of the r_ε ratio along x observed in domain $\mathcal{D}_2$. As an example, this is the value of the summit of the curves in Figure 11. This enabled us to plot this maximum value as a function of ℓ_2 for various values of r_E. These curves are shown in Figure 12. It can be seen that depending on the value of r_E, a damping of 10 % of the strain peak in $\mathcal{D}_2$ is obtained for a value of ℓ_2 lying between 0.1 and 0.35 mm: the higher the value of r_E, thus the more pronounced the strain increase in $\mathcal{D}_2$, the lower this threshold value for ℓ_2, which seems logical.

The results obtained with the tests above can be discussed through the prism of this model, especially Test #1 for which the jumps in the strain maps are more pronounced. Points A, B and C

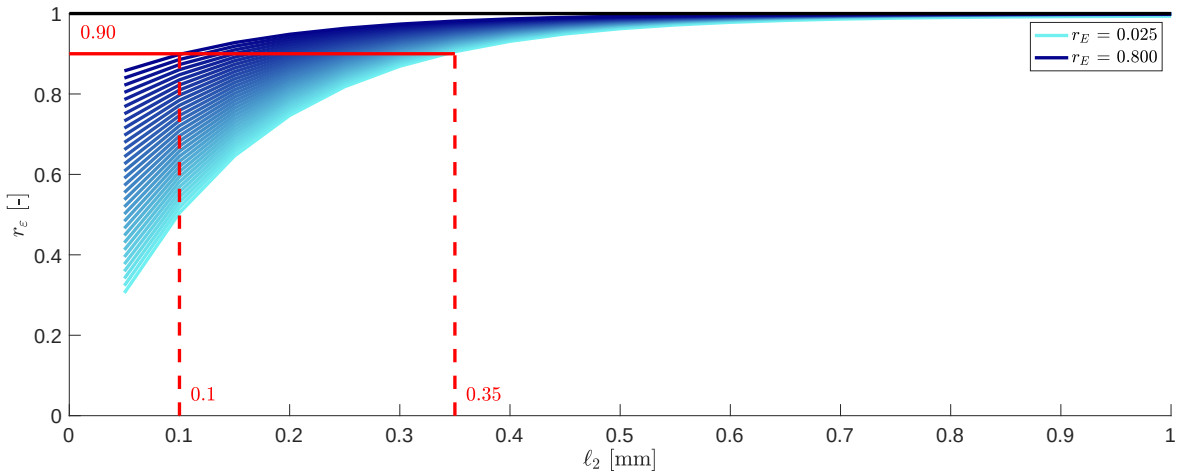

Figure 12: Maximum value of the $r_\varepsilon = \frac{E_2 \varepsilon_{xx}^{(g_i)}}{\sigma_{xx}^{\infty}}$ ratio in domain $\mathcal{D}_2$ for various r_E ratios (between 0.025 and 0.800) and values of ℓ_2 (between 0.1 and 1 mm).

in Figure 6-(a) show that the strain distribution abruptly stops at the border of CKB #1, while their prolongations at the other side progressively stop (Points A', B' and C'). This illustrates the effect of the transfer zone described by the 1D model at the free borders. The 1D model predicts that the transfer zone, here estimated by considering it is defined by the abscissa for which 90 % of the plateau value observed in Figure 11 in $\mathcal{D}_1$ is reached, has a length equal to 0.2 [mm] (see left-hand side of Figure 11). Figure 6-(a) shows that the progressive loading of the optical strain gage along its border is somewhat longer, say approximately between 0.5 and 1 [mm] at Points A', B' and C'. This figure depicts the ε_{xy} distribution and not the longitudinal strain along the bands, which would undoubtedly be more representative for a comparison with a 1D model. Still, the three in-plane strain components are all affected similarly. This transfer length fluctuates from one band to another, which is probably because the thickness of the glue is not constant or because the excess glue along the boundary does not form the same glue border everywhere after polymerization. However, it can be said that the order of magnitude of this transfer length observed experimentally is greater than that predicted by the model. This difference is certainly caused by the different assumptions under which the calculations are performed: the value of the different parameters, which are approximated, and the fact that this is a 1D and, not a 2D model. However, this greater experimental transfer length lends credence to the

fact that tiny details as small as those observed in the martensite laminates with CKB #1, see red box in Figure 4-(b) (their period is equal to about $\simeq$14 [px]$\times$7.2 [μm/px]$\simeq$ 100 [μm] = 0.1 [mm]), cannot be revealed by CKB #2 because of the damping effect of the optical strain gage. This point should, however, be investigated further with dedicated experiments.

e_s [mm]	e_a [mm]	e_g [mm]	ℓ_1 [mm]	ℓ_2 [mm]	E_1 [GPa]	E_2 [GPa]	G_a [GPa]	E_g [GPa]
3	0.005	0.025	50	1 to 10	120	5	0.46	6

Table 2: Values of the parameters governing the shear lag model

Conclusion

A procedure for laser-engraving checkerboard patterns on polyimide films as thin as 25 microns is proposed in this paper. It is shown that such laser-engraved films form an optical strain gage that can be bonded on flat specimens by using a procedure similar to that used to glue electric strain gages, mainly because polyimide films frequently constitute the backing material of this classic measuring device. The difference with the latter is twofold. First, the polyimide film employed here is white in its bulk instead of brown to ensure good contrast with the dots forming the checkerboard pattern. Second, the present optical gage returns the full-field strain distribution beneath the optical strain gage instead of the mean strain value under the resistance returned by electric gages. The strain maps obtained in two different testing configurations show that only negligible differences can be detected compared to strain maps returned by the procedure used so far to deposit optimized patterns, which consists of spray-painting the specimen, and then directly engraving the paint layer with the same type of engraver as that used in this study. Tiny details are revealed in the strain maps that are shown. This illustrates that this optical strain gage can be an ideal tool for analyzing heterogeneous strain fields in experimental mechanics. In addition, images are processed with a spectral technique and not with digital image correlation. The former technique is much more computationally demanding, which enables us to provide pixelwise-defined strain maps.

Some points should be investigated further to improve the quality and reliability of the measure-

ments provided by this optical strain gage. For instance, the quality of the laser-engraved checkerboard patterns depends on several parameters, and the optimal settings found for them in this study could be improved by testing other combinations of these multiple parameters. Thinner films and other types of polymeric films should also be tested. Dedicated experiments should also be designed and performed to apply on the optical strain gage the stereo-LSA technique recently introduced in [42], or to finely validate the 1D model proposed in this study.

However, this study already opens up two perspectives. First, demonstrating that the optimal pattern for full-field strain measurement, namely checkerboards with a tiny pitch for zones of interest of several cm^2, can be deposited on thin polyimide layers makes it possible to pre-print such patterns on an industrial scale like classic electric strain gages routinely employed in industry. This would make this type of gage affordable and commercially available. Second, the geometry of a checkerboard pattern is easy to define, for instance, by giving the value of the size of the unit dots forming the pattern, the tilt angle when taking the images, or the number of pixels per period that should ideally be employed to encode the periodic pattern in digital images. A consequence is that checkerboard patterns would be easy to standardize. These two perspectives certainly deserve to be explored in the future. This would help spread and popularize optimal patterns for full-field strain measurement in the experimental mechanics community and contribute to making such measurements more reliable and reproducible.

Acknowledgements

Mr. Jacques, from the ADDEV Materials company, Saint-Chamond, France (`https://addevmaterials.com/en/`), is gratefully acknowledged for providing the white polyimide film used to prepare the optical strain gages tested in this study, and Pr. Jean-Benoît Le Cam for supplying silicone plates during the development of the bonding procedure of the gage.

Appendix 1: Procedure and settings used for engraving the checkerboard pattern on the paint or on the polyimide film

The procedure consists first of cutting a piece of white polyimide strip and placing it in the chamber of the laser marker. The laser marker used in this paper is the MDU1000C marker made by Keyence. The checkerboard pattern is then engraved on this film using the same procedure as that described in [18]. Four parameters directly influence the quality of the resulting pattern:

1. Scan speed: This is the movement speed of the laser spot. Its maximum value is 12,000 mm/s. This is quite high, but it is worth remembering that no mechanical system is involved, thus no inertia effect may slow down this movement.
2. Pulse frequency: This is the frequency at which a pulse is emitted by the system. The higher this frequency, the lower the spot energy. This quantity lies between 40 and 400 kHz.
3. Repetition: This is the number of passes of the laser, that is, the number of times the same pattern is printed at the same place. The higher this number, the more marked the contrast of the resulting pattern, but this number must also be limited in the present case to avoid piercing the film, or to pierce it with the smallest possible holes.
4. Laser power: The maximum power is equal to 3 W at 40 kHz, but the value at the focal point is 2.5 W only. The laser power can be adjusted between 0 and 100 % of this maximum value.

A fifth parameter can be mentioned, namely the spot variable. This setting corresponds to a slight defocus, but this option was not used in the present study.

	Paint (SMA)	**Paint (wood)**	**Polyimide**
Scan speed [mm/s]	3600	3600	3600
Pulse frequency [kHz]	60	60	60
Number of repetitions [-]	35	40	35
Percentage of laser power [-]	50%	80%	80%

Table 3: Settings used for engraving the checkerboard patterns on the two specimens tested in this study.

Appendix 2: Shear lag model

Assumptions

The objective here is to model the 1D stress and strain distributions along an optical strain gage bonded on a substrate. The latter is split into three zones, namely $\mathcal{D}_1$, $\mathcal{D}_2$ and $\mathcal{D}_3$ (see Figure 10). The latter domain is mirror-symmetric to $\mathcal{D}_1$ with respect to the midline Δ of $\mathcal{D}_2$.

The assumptions under which the calculations are performed are the same as those employed in the shear lag model presented first in the seminal paper by Volkersen [41]. The only difference is the fact that the substrate is divided into three zones, while classic shear lag models focus on the transfer zone at the free edge of a unique zone. These assumptions are as follows:

- The model for the stress distribution in the substrate, the adhesive, and the optical strain gage is unidimensional.
- Traction is applied on the left- and right-hand sides of the substrate. Its intensity is denoted by σ_{xx}^{∞}.
- The substrate and the optical strain gage are subjected to normal stress along x only, and the adhesive to shear stress only. Their distributions over $\mathcal{D}_1$ and $\mathcal{D}_2$ are respectively denoted by $\sigma_{xx}^{(s_i)}$, $\sigma_{xx}^{(g_i)}$, and $\sigma_{xz}^{(a_i)}$, $i \in 1, 2$. The distributions over $\mathcal{D}_3$ will be deduced by mirror-symmetry from their counterparts calculated over $\mathcal{D}_1$.

- The constitutive material of the three components is linear elastic. The Young's modulus of the film used for the optical strain gage is denoted by E_g, the Young's modulus of the substrate by E_{S_1} and E_{S_2} over domains $\mathcal{D}_1$ and $\mathcal{D}_2$, respectively. The shear modulus of the adhesive is denoted by G_a. e_s, e_a, and e_g represent the thickness of the substrate, the adhesive and the optical strain gage, respectively.

The model that is developed below should also satisfy the four conditions listed below (three boundary conditions and a symmetry condition):

- BC1: The boundary of the optical strain gage is free at $x = 0$
- BC2: The normal stress distribution in the optical strain gage is continuous at $x = \ell_1$
- BC3: The shear stress distribution in the adhesive is continuous at $x = \ell_1$.

in addition to giving a solution that is strictly symmetric with respect to the middle of $\mathcal{D}_2$.

Development of the model

The equilibrium of the small portion of substrate over $\mathcal{D}_1$ shown in Figure 10-b reads as follows:

$$\left(-\sigma_{xx}^{(s_1)} + \sigma_{xx}^{(s_1)} + d\sigma_{xx}^{(s_1)}\right) e_s + \sigma_{xz}^{(a_1)} dx = 0 \tag{4}$$

Thus,

$$\frac{d\sigma_{xx}^{(s_1)}}{dx} e_s + \sigma_{xz}^{(a_1)} = 0. \tag{5}$$

In the same way, we have for the portion of the optical strain gage:

$$\left(-\sigma_{xx}^{(g_1)} + \sigma_{xx}^{(g_1)} + d\sigma_{xx}^{(g_1)}\right) e_g - \sigma_{xz}^{(a_1)} dx = 0, \tag{6}$$

which gives

$$\frac{d\sigma_{xx}^{(g_1)}}{dx} e_g - \sigma_{xz}^{(a_1)} = 0. \tag{7}$$

Substituting $\sigma_{xz}^{(a_1)}$ from Equation 5 in Equation 7 leads to:

$$\frac{d}{dx}\left(\sigma_{xx}^{(s_1)}e_s + \sigma_{xx}^{(g_1)}e_g\right) = 0. \tag{8}$$

Integrating with respect to x and considering the boundary conditions of domain $\mathcal{D}_1$ leads to:

$$\sigma_{xx}^{(s_1)}e_s + \sigma_{xx}^{(g_1)}e_g = \sigma_{xx}^{(s)\infty}e_s. \tag{9}$$

Thus

$$\sigma_{xx}^{(s_1)} = \sigma_{xx}^{(s)\infty} - \sigma_{xx}^{(g_1)}\frac{e_g}{e_s}. \tag{10}$$

The thickness of the adhesive layer is small, so the through-thickness engineering shear strain $\gamma_{xz}^{(a_1)}$ is reasonably assumed to be homogeneous, which enables us to express it as a function of the displacement along x in the film ($u_x^{(g_1)}$) and in the substrate ($u_x^{(s_1)}$):

$$\gamma_{xz}^{(a_1)} = \frac{u_x^{(g_1)} - u_x^{(s_1)}}{e_a}. \tag{11}$$

The adhesive is linear elastic, thus

$$\sigma_{xz}^{(a_1)} = G_a\gamma_{xz}^{(a_1)} = G_a\frac{u_x^{(g_1)} - u_x^{(s_1)}}{e_a}. \tag{12}$$

Substituting this expression of $\sigma_{xz}^{(a_1)}$ in Equation 7 leads to:

$$\frac{d\sigma_{xx}^{(g_1)}}{dx}e_g - \frac{G_a}{e_a}\left(u_x^{(g_1)} - u_x^{(s_1)}\right) = 0. \tag{13}$$

This equation is then derivated with respect to x, which gives:

$$\frac{d^2\sigma_{xx}^{(g_1)}}{dx^2}e_g - \frac{G_a}{e_a}\left(\varepsilon_{xx}^{(g_1)} - \varepsilon_{xx}^{(s)}\right) = 0. \tag{14}$$

Since $\varepsilon_{xx}^{(g_1)} = \dfrac{\sigma_{xx}^{(g_1)}}{E_g}$ and $\varepsilon_{xx}^{(s_1)} = \dfrac{\sigma_{xx}^{(s_1)}}{E_{s_1}}$, Equation 14 becomes:

$$\frac{d^2\sigma_{xx}^{(g_1)}}{dx^2}e_g - \frac{G_a}{e_a}\left(\frac{\sigma_{xx}^{(g_1)}}{E_g} - \frac{\sigma_{xx}^{(s_1)}}{E_{s_1}}\right) = 0. \tag{15}$$

After introducing in the preceding equation the expression of $\sigma_{xx}^{(s_1)}$ given in Equation 10 and dividing by e_g, we have

$$\frac{d^2\sigma_{xx}^{(g_1)}}{dx^2} - \frac{G_a}{e_a}\left(\frac{1}{e_g E_g} + \frac{1}{e_s E_{s_1}}\right)\sigma_{xx}^{(g_1)} + \frac{G_a}{e_a e_g E_{s_1}}\sigma_{xx}^{\infty} = 0. \tag{16}$$

The same reasoning can be applied to domain $\mathcal{D}_2$, thus

$$\frac{d^2\sigma_{xx}^{(g_2)}}{dx^2} - \frac{G_a}{e_a}\left(\frac{1}{e_g E_g} + \frac{1}{e_s E_{s_2}}\right)\sigma_{xx}^{(g_2)} + \frac{G_a}{e_a e_g E_{s_2}}\sigma_{xx}^{\infty} = 0. \tag{17}$$

In conclusion, the stress distribution in the optical strain gage is modeled by the following two differential equations:

$$\begin{cases} \dfrac{d^2\sigma_{xx}^{(g_1)}}{dx^2} - (\gamma_1)^2\,\sigma_{xx}^{(g_1)} = -\beta_1 \quad \text{over } \mathcal{D}_1 \\ \dfrac{d^2\sigma_{xx}^{(g_2)}}{dx^2} - (\gamma_2)^2\,\sigma_{xx}^{(g_2)} = -\beta_2 \quad \text{over } \mathcal{D}_2 \end{cases} \tag{18}$$

with :

$$\begin{cases} \beta_1 = \dfrac{G_a}{e_a e_g E_{s_1}}\sigma_{xx}^{\infty} & \beta_2 = \dfrac{G_a}{e_a e_g E_{s_2}}\sigma_{xx}^{\infty} \\ \gamma_1 = \sqrt{\dfrac{G_a}{e_a}\left(\dfrac{1}{e_g E_g} + \dfrac{1}{e_s E_{s_1}}\right)} & \gamma_2 = \sqrt{\dfrac{G_a}{e_a}\left(\dfrac{1}{e_g E_g} + \dfrac{1}{e_s E_{s_2}}\right)} \end{cases}. \tag{19}$$

We now give the solutions of these two differential equations by using the classic resolution method of linear differential equations of second order and first degree.

Solution of the associated homogeneous equation. The roots of the characteristic polynomial of these equations are γ_1 and $-\gamma_1$ for the former, and γ_2 and $-\gamma_2$ for the latter, so the solutions of the homogeneous equations associated to the two complete equations read as follows:

$$\begin{cases} \sigma_{xx}^{(g_1)} = K_1 e^{\gamma_1 x} + L_1 e^{-\gamma_1 x} \quad K_1, L_1 \in \mathbb{R} \\ \sigma_{xx}^{(g_2)} = K_2 e^{\gamma_2 x} + L_2 e^{-\gamma_2 x} \quad K_2, L_2 \in \mathbb{R}. \end{cases} . \tag{20}$$

Particular solution of the complete equation. $\sigma_{xx}^{(g_1)} = k_1$, $\sigma_{xx}^{(g_2)} = k_2$ are particular solutions of the complete equations. Feeding the complete differential equations with these particular expressions of $\sigma_{xx}^{(g_1)}$ and $\sigma_{xx}^{(g_2)}$ leads to $k_1 = \frac{\beta_1}{\gamma_1^2}$ and $k_2 = \frac{\beta_2}{\gamma_2^2}$.

Solution of the complete equation. The solution of each equation is obtained by adding the last two expressions, thus:

$$\begin{cases} \sigma_{xx}^{(g_1)} = K_1 e^{\gamma_1 x} + L_1 e^{-\gamma_1 x} + \dfrac{\beta_1}{\gamma_1^2} \\ \sigma_{xx}^{(g_2)} = K_2 e^{\gamma_2 x} + L_2 e^{-\gamma_2 x} + \dfrac{\beta_2}{\gamma_2^2} \end{cases} . \tag{21}$$

Fixing the value of K_1, K_2, L_1 and L_2. The four conditions listed above give equations that are now used to fix the value of K_1, K_2, L_1 and L_2

- BC1 (the boundary of the optical strain gage is free at $x = 0$): $\sigma_{xx}^{(g_1)}(0) = 0$
- BC2 (the normal stress distribution in the optical strain gage is continuous at $x = \ell_1$): $\sigma_{xx}^{(g_1)}(\ell_1) = \sigma_{xx}^{(g_2)}(\ell_1)$
- BC3 (the shear stress distribution in the adhesive $\sigma_{xz}^{(a)}$ is continuous at $x = \ell_1$): $\dfrac{d\sigma_{xx}^{(g_1)}}{dx}(\ell_1) = \dfrac{d\sigma_{xx}^{(g_2)}}{dx}(\ell_1)$ according to Equation 7
- mirror-symmetry condition (the normal stress distribution in the optical strain gage is symmetric at $x = \ell_1 + \dfrac{\ell_2}{2}$): $\dfrac{d\sigma_{xx}^{(g_2)}}{dx}(\ell_1 + \dfrac{\ell_2}{2}) = 0$

This leads to the following linear system:

$$\begin{cases} K_1 + L_1 = -\dfrac{\beta_1}{\gamma_1^2} \\ K_1 e^{\gamma_1 \ell_1} + L_1 e^{-\gamma_1 \ell_1} - K_2 e^{\gamma_2 \ell_1} - L_2 e^{-\gamma_2 \ell_1} = -\dfrac{\beta_1}{\gamma_1^2} + \dfrac{\beta_2}{\gamma_2^2} \\ \gamma_1 K_1 e^{\gamma_1 \ell_1} - \gamma_1 L_1 e^{-\gamma_1 \ell_1} - \gamma_2 K_2 e^{\gamma_2 \ell_1} + \gamma_2 L_2 e^{-\gamma_2 \ell_1} = 0 \\ K_2 e^{\gamma_2 \left(\ell_1 + \frac{\ell_2}{2}\right)} + L_2 e^{-\gamma_2 \left(\ell_1 + \frac{\ell_2}{2}\right)} = 0 \end{cases} . \tag{22}$$

This system of four linear equations was inverted with XCAS, an open-source symbolic computation software [43]. After reordering the raw results, the following expressions were obtained for K_1, L_1, K_2 and L_2:

$$\begin{cases} K_1 = \dfrac{\mathrm{e}^{\gamma_2\ell_2}\left[-\beta_1\gamma_1\gamma_2 + \beta_1\gamma_2^2\left(1-\mathrm{e}^{\gamma_1\ell_1}\right) + \beta_2\gamma_1^2\mathrm{e}^{\gamma_1\ell_1}\right] - \beta_1\left(\gamma_1\gamma_2 - \gamma_2^2\mathrm{e}^{\gamma_1\ell_1} + \gamma_2^2\right) - \beta_2\gamma_1^2\mathrm{e}^{\gamma_1\ell_1}}{\gamma_1^3\gamma_2\left[\left(\mathrm{e}^{\gamma_2\ell_2}+1\right)\left(\mathrm{e}^{2\gamma_1\ell_1}+1\right)\right] + \gamma_1^2\gamma_2^2\left[\left(\mathrm{e}^{\gamma_2\ell_2}-1\right)\left(\mathrm{e}^{2\gamma_1\ell_1}-1\right)\right]} \\ K_2 = \dfrac{\left(\beta_1\gamma_2^2\mathrm{e}^{2\gamma_1\ell_1} - 2\beta_1\gamma_2^2\mathrm{e}^{\gamma_1\ell_1} + \beta_1\gamma_2^2 - \beta_2\gamma_1^2\mathrm{e}^{2\gamma_1\ell_1} - \beta_2\gamma_1^2\right)\mathrm{e}^{\gamma_2\ell_1}}{\gamma_2^2\gamma_1\left[\left(\mathrm{e}^{2\gamma_1\ell_1}\mathrm{e}^{2\gamma_2\ell_1} + \mathrm{e}^{2\gamma_2\ell_1+\gamma_2\ell_2}\right)\left(\gamma_1-\gamma_2\right) + \left(\mathrm{e}^{2\gamma_1\ell_1}\mathrm{e}^{2\gamma_2\ell_1+\gamma_2\ell_2} + \mathrm{e}^{2\gamma_2\ell_1}\right)\left(\gamma_2+\gamma_1\right)\right]} \\ L_1 = -\dfrac{\mathrm{e}^{\gamma_1\ell_1}\left[\beta_1\gamma_1\gamma_2\left(\mathrm{e}^{\gamma_2\ell_2}\mathrm{e}^{\gamma_1\ell_1} + \mathrm{e}^{\gamma_1\ell_1}\right) + \beta_1\gamma_2^2\left(\mathrm{e}^{\gamma_2\ell_2}\mathrm{e}^{\gamma_1\ell_1} - \mathrm{e}^{\gamma_2\ell_2} - \mathrm{e}^{\gamma_1\ell_1} + 1\right) + \gamma_1^2\beta_2\left(\mathrm{e}^{\gamma_2\ell_2} - 1\right)\right]}{\gamma_1^3\gamma_2\left[\left(\mathrm{e}^{\gamma_2\ell_2}+1\right)\left(\mathrm{e}^{2\gamma_1\ell_1}+1\right)\right] + \gamma_1^2\gamma_2^2\left[\left(\mathrm{e}^{\gamma_2\ell_2}-1\right)\left(\mathrm{e}^{2\gamma_1\ell_1}-1\right)\right]} \\ L_2 = \dfrac{\mathrm{e}^{2\gamma_2\ell_1+\gamma_2\ell_2}\mathrm{e}^{\gamma_2\ell_1}\left[\beta_1\gamma_2^2\left(\mathrm{e}^{\gamma_1\ell_1}-1\right)^2 - \beta_2\gamma_1^2\left(\mathrm{e}^{2\gamma_1\ell_1}+1\right)\right]}{\gamma_2^2\gamma_1\left[\left(\mathrm{e}^{2\gamma_1\ell_1}\mathrm{e}^{2\gamma_2\ell_1} + \mathrm{e}^{2\gamma_2\ell_1+\gamma_2\ell_2}\right)\left(\gamma_1-\gamma_2\right) + \left(\mathrm{e}^{2\gamma_1\ell_1}\mathrm{e}^{2\gamma_2\ell_1+\gamma_2\ell_2} + \mathrm{e}^{2\gamma_2\ell_1}\right)\left(\gamma_2+\gamma_1\right)\right]} \end{cases} \tag{23}$$

The model is unidimensional, so the strain distribution along the optical strain gage is merely obtained by dividing the stress distribution by the value of the Young's modulus over each of the two domains $\mathcal{D}_1$ and $\mathcal{D}_2$. Thus:

$$\begin{cases} \varepsilon_{xx}^{(g_1)} = \dfrac{1}{E_1}\left(K_1 e^{\gamma_1 x} + L_1 e^{-\gamma_1 x} + \dfrac{\beta_1}{\gamma_1^2}\right) \\ \varepsilon_{xx}^{(g_2)} = \dfrac{1}{E_2}\left(K_2 e^{\gamma_2 x} + L_2 e^{-\gamma_2 x} + \dfrac{\beta_2}{\gamma_2^2}\right) \end{cases}. \tag{24}$$

In conclusion, the strain distribution along the optical strain gage over $\mathcal{D}_1$ and $\mathcal{D}_2$ is given by Equations 24 above. Coefficients K_1, K_2, L_1 and L_2 are given by Equations 23, and coefficients β_1, β_2, γ_1 and γ_2 by Equations 19. The strain distribution along the optical strain gage over $\mathcal{D}_3$ is mirror-symmetric to its counterpart over $\mathcal{D}_1$. This gives Equation 3 in Section 4.

References

[1] M. A. Sutton, J.-J. Orteu, and H. Schreier. Image Correlation for Shape, Motion and Deformation Measurements: Basic Concepts,Theory and Applications. Springer, 2009. 364 pages. ISBN: 978-0-387-78746-6.

[2] S. Bossuyt. Optimized patterns for digital image correlation. In Conference Proceedings of the Society for Experimental Mechanics Series, volume 3, pages 239–248, 2013.

[3] G. F. Bomarito, J. D. Hochhaltera, T. J. Rugglesb, and A. H. Cannon. Increasing accuracy and precision of digital image correlation through pattern optimization. Optics and Lasers in Engineering, 91(April):73–85, 2017.

[4] G. F. Bomarito, J. D. Hochhalter, T. J. Ruggles, and A. H. Cannon. Increasing accuracy and precision of digital image correlation through pattern optimization. Optics and Lasers in Engineering, 91(May 2016):73–85, 2017.

[5] Y. Su, Q. Zhang, and Z. Gao. Statistical model for speckle pattern optimization. Optics Express, 25(24):30259–30275, Nov 2017.

[6] A. Lavatelli, R. Balcaen, E. Zappa, and D. Debruyne. Closed-loop optimization of DIC speckle patterns based on simulated experiments. IEEE Transactions on Instrumentation and Measurement, 68(11):4376–4386, 2019.

[7] M. Mathew, B. Wisner, S. Ridwan, M. McCarthy, I. Bartoli, and A. Kontsos. A Bio-Inspired Frequency-Based Approach for Tailorable and Scalable Speckle Pattern Generation. Experimental Mechanics, 60(8):1103–1117, 2020.

[8] R. Fouque, R. Bouclier, J.C. Passieux, and J.N. Périé. Fractal pattern for multiscale digital image correlation. Experimental Mechanics, 61(3):483–497, 2021.

[9] C. C. K. Chan, D. Kumar, and C-H. Chiang. Coarse and fine localized CNN classifier for intelligent DIC preprocessing in large structure health monitoring sample. In Tzu-Yang Yu and

Andrew L. Gyekenyesi, editors, Nondestructive Characterization and Monitoring of Advanced Materials, Aerospace, Civil Infrastructure, and Transportation XV, volume 11592, pages 141 – 152. International Society for Optics and Photonics, SPIE, 2021.

[10] Y. Wang, Y. Gao, Y. Liu, Z. Gao, Y. Su, and Q. Zhang. Optimal aperture and digital speckle optimization in digital image correlation. Experimental Mechanics, 61(4):677–684, 2021.

[11] Y. Shi, B. Blaysat, H. Chanal, and M. Grédiac. Designing patterns for DIC with Poisson image editing. Experimental Mechanics, 62(7):1093–1117, 2022.

[12] M. Grédiac, B. Blaysat, and F. Sur. A critical comparison of some metrological parameters characterizing local digital image correlation and grid method. Experimental Mechanics, 57(6):871–903, 2017.

[13] M. Grédiac, B. Blaysat, and F. Sur. On the Optimal Pattern for Displacement Field Measurement: Random Speckle and DIC, or Checkerboard and LSA? Experimental Mechanics, 60(4):509–534, 2020.

[14] M. Grédiac, F. Sur, and B. Blaysat. Comparing several spectral methods used to extract displacement and strain fields from checkerboard images. Optics and Lasers in Engineering, 127:105984, 2020.

[15] M. J. Hÿtch, E. Snoeck, and R. Kilaas. Quantitative measurement of displacement and strain fields from HREM micrographs. Ultramicroscopy, 74:131–146, 1998.

[16] X. Dai, H. Xie, and H. Wang. Geometric phase analysis based on the windowed fourier transform for the deformation field measurement. Optics and Laser Technology, 58(6):119–127, 2014.

[17] J.L. Piro and M. Grédiac. Producing and transferring low-spatial-frequency grids for measuring displacement fields with moiré and grid methods. Experimental Techniques, 28(4):23–26, 2004.

[18] Q. Bouyra, B. Blaysat, H. Chanal, and M. Grédiac. Using laser marking to engrave optimal patterns for in-plane displacement and strain measurement. Strain, 58(2):e12404, 2022.

[19] A. Vinel, M. Laquet, X. Balandraud, B. Blaysat, M. Grédiac, and T. Jailin. Full-field strain investigation of martensite twins in thermally activated Cu-Al-Ni single crystal by Localized Spectrum Analysis. Acta Materiallia, 264:119550, 2024.

[20] F. Pierron and M. Grédiac. Towards Material Testing 2.0. a review of test design for identification of constitutive parameters from full-field measurements. Strain, 57(1):e12370, 2021.

[21] F. Pierron. Material Testing 2.0: A brief review. Strain, 59(3):e12434, 2023.

[22] du Pont de Nemours. New Kapton® WS Series Product Family.

[23] F. Sur, B. Blaysat, and M. Grédiac. Characterizing the measurement resolution and measurement bias of sampling moiré. Optics and Lasers in Engineering, 2023. In revision.

[24] M. Grédiac, F. Sur, and B. Blaysat. The grid method for in-plane displacement and strain measurement: a review and analysis. Strain, 52(3):205–243, 2016.

[25] M. Grédiac, B. Blaysat, and F. Sur. Extracting displacement and strain fields from checkerboard images with the localized spectrum analysis. Experimental Mechanics, 59(2):207–218, 2019.

[26] F. Sur and M. Grédiac. Influence of the analysis window on the metrological performance of the grid method. Journal of Mathematical Imaging and Vision, 56(3):472–498, 2016.

[27] F. Sur and M. Grédiac. Towards deconvolution to enhance the grid method for in-plane strain measurement. Inverse Problems and Imaging, 8(1):259–291, 2014. American Institute of Mathematical Sciences.

[28] M. Grédiac, B. Blaysat, and F. Sur. A robust-to-noise deconvolution algorithm to enhance displacement and strain maps obtained with local DIC and LSA. Experimental Mechanics, 59(2):219–243, 2019.

[29] M. Grédiac, X. Balandraud, B. Blaysat, T. Jailin, R. Langlois, F. Sur, and A. Vinel. Fine-tuning a deconvolution algorithm to restore displacement and strain maps obtained with lsa. Experimental Mechanics, 63(9):1509–1537, 2023.

[30] B. Blaysat, M. Grédiac, T. Jailin, and F. Sur. OpenLSA: open-source toolbox for computing full-field displacements from images of periodic patterns. 2024.

[31] F. Sur, B. Blaysat, and M. Grédiac. Determining displacement and strain maps immune from aliasing effect with the grid method. Optics and Lasers in Engineering, 86:317–328, 2016.

[32] G.E. Healey and R. Kondepudy. Radiometric ccd camera calibration and noise estimation. IEEE Transactions on Pattern Analysis and Machine Intelligence, 16(3):267–276, 1994.

[33] A. Foi, M. Trimeche, V. Katkovnik, and K. K. Egiazarian. Practical Poissonian-Gaussian noise modeling and fitting for single-image raw-data. IEEE Transactions on Image Processing, 17(10):1737–1754, 2008.

[34] M. Grédiac and F. Sur. Effect of sensor noise on the resolution and spatial resolution of the displacement and strain maps obtained with the grid method. Strain, 50(1):1–27, 2014. Paper invited for the 50th anniversary of the journal. Wiley.

[35] S. Qin, M. Grédiac, B. Blaysat, S. Ma, and F. Sur. Influence of the sampling density on the noise level in displacement and strain maps obtained by processing periodic patterns. Measurement, 173:108570, 2021.

[36] F. Sur and M. Grédiac. On noise reduction in strain maps obtained with the grid method by averaging images affected by vibrations. Optics and Lasers in Engineering, 66:210–222, 2015.

[37] E. W. Grafarend. Linear and Nonlinear Models: Fixed Effects, Random Effects, and Mixed Models. Walter de Gruyter, 2006.

[38] M. Grédiac, B. Blaysat, and F. Sur. A critical comparison of some metrological parameters characterizing local digital image correlation and grid method. Experimental Mechanics, 57(3):871–903, 2017.

[39] S. Stupkiewicz, G. Maciejewski, and H. Petryk. Low-energy morphology of the interface layer between austenite and twinned martensite. Acta Materiali, 55:6292–6306, 2007.

[40] MatWeb. Material property data. https://www.matweb.com/search/datasheettext.aspx?matguid=d0d7dbec7666421c

[41] O. Volkersen. Die Nietkraftverteilung in zugbeanspruchten Nietverbindungen mit konstanten Laschenquerschnitten. Luftfahrtforschung, 15:41–47, 1938.

[42] T. Jailin, B. Blaysat, A. Vinel, R. Langlois, and M. Grédiac. Stereo-measurements on optimal patterns based on localised spectrum analysis. 2024. to be submitted.

[43] XCAS, the Swiss army knife of mathematics. `https://xcas.univ-grenoble-alpes.fr/en.html`. Available online.